UC San Diego
UC San Diego Previously Published Works

Title
Coastal Stratocumulus Dissipation Dependence on Initial Conditions and Boundary Forcings in a Mixed-Layer Model

Permalink
https://escholarship.org/uc/item/26j9c40r

Journal
Journal of the Atmospheric Sciences, 77(8)

ISSN
0022-4928

Authors
Zapata, Mónica Zamora
Norris, Joel R
Kleissl, Jan

Publication Date
2020-08-01

DOI
10.1175/jas-d-19-0254.1

Peer reviewed

eScholarship.org Powered by the California Digital Library
University of California

Coastal stratocumulus dissipation dependence on initial conditions and boundary forcings in a Mixed-Layer Model

Mónica Zamora Zapata*

Department of Mechanical and Aerospace Engineering, University of California, San Diego, La Jolla, California

Joel R. Norris

Scripps Institution of Oceanography, University of California, San Diego, La Jolla, California

Jan Kleissl

Department of Mechanical and Aerospace Engineering, University of California, San Diego, La Jolla, California

**Corresponding author address:* Mónica Zamora Zapata, Department of Mechanical and Aerospace Engineering, University of California, San Diego, La Jolla, California

E-mail: mzamoraz@eng.ucsd.edu

ABSTRACT

The impact of initial states and meteorological variables on stratocumulus cloud dissipation time over coastal land is investigated using a Mixed-Layer Model. A large set of realistic initial conditions and forcing parameters are derived from radiosonde observations and Numerical Weather Prediction model outputs, including: total water mixing ratio and liquid water potential temperature profiles (within the boundary layer, across the capping inversion, and at 3 km), inversion base height and cloud thickness, large-scale divergence, wind speed, Bowen ratio, sea surface fluxes, sky effective radiative temperature, shortwave irradiance above the cloud, and sea level pressure. We study the sensitivity of predicted dissipation time using two analyses. In the first, we simulate 195 cloudy days (all variables co-vary as observed in nature). We caution that simulated predictions correlate only weakly to observations of dissipation time, but the simulation approach is robust and facilitates co-variability testing. In the second, a single variable is varied around an idealized reference case. While both analyses agree in that initial conditions influence dissipation time more than forcing parameters, some results with co-variability differ greatly from the more traditional sensitivity analysis and with previous studies: opposing trends are observed for boundary layer total water mixing ratio and Bowen ratio, and co-variability diminishes the sensitivity to cloud thickness and inversion height by a factor of five. With co-variability, the most important features extending predicted cloud lifetime are (i) initially thicker clouds, higher inversion height, and stronger temperature inversion jumps, and (ii) boundary forcings of lower sky effective radiative temperature.

1. Introduction

Marine stratocumulus (Sc) clouds cover a large area of the planet at the eastern side of oceans where upwelling keeps the sea colder and at latitudes where the subsiding branch of the Hadley cell pushes the atmospheric boundary layer (ABL) down and caps it with warm air, creating an inversion layer that limits the vertical cloud extent. The main physical processes controlling the evolution of Sc clouds are radiation, turbulence, surface fluxes, entrainment, and precipitation (Wood 2012; Stevens 2004; Nieuwstadt and Duynkerke 1996). Sc clouds are maintained by convective turbulent motions, driven mainly by cloud-top radiative cooling that generates sinking plumes and cools the ABL (Lilly 1968). The turbulent motions allow water vapor from the surface to mix and rise up to the condensation level to form a cloud. Near the top of the cloud, there is a complex interface zone exposed to entrainment of air from the free troposphere (Mellado 2017).

Marine Sc clouds have a net cooling effect on the planet (Hartmann et al. 1992) and their impact under climate change conditions is still a matter of research (Zelinka et al. 2017; Bony and Dufresne 2005; Duynkerke and Teixeira 2001). Coastal cities near Sc regions are affected by their presence— not only in terms of climate, but also from the perspective of solar energy generation. As solar heating overcomes cloud-top radiative cooling, clouds over land thin during the day, warming the ABL and changing its turbulent structure (Fang et al. 2014). No solar radiation is present during the night, resulting in more effective radiative cooling, which causes cloud growth. During the day, solar electricity generation ramps up as Sc clouds dissipate in the morning hours (Jamaly et al. 2013; Wellby and Engerer 2015) or an extended shortfall of solar generation occurs when Sc clouds persist for the whole day. A better understanding of Sc cloud dissipation can help improve solar energy forecasting in these regions.

Different physical processes and meteorological parameters affect the inland coverage of marine Sc clouds and the dissipation time over coastal land. For marine clouds, some parameters have been linked to decreased cloudiness: greater sea surface temperatures (SST) (Hanson 1990; Seethala et al. 2015), weaker lower tropospheric stability (LTS) (Klein and Hartmann 1993; Wood and Bretherton 2006; Klein et al. 1995), weaker horizontal cold-air advection, weaker surface wind speed, a moister free-troposphere, and lower sea level pressure (SLP) (Klein et al. 1995; Seethala et al. 2015). Research has been less extensive over coastal land, where earlier dissipation has been linked to smaller Bowen ratio Bo (the ratio between sensible and latent heat fluxes over land) and weaker sea-breeze advection using simple sensitivity analyses (Ghonima et al. 2016; Akyurek and Kleissl 2017).

Most factors do not contribute independently to cloud dissipation because they are inter-related with other variables and co-vary in nature. Some variables co-vary due to the nature of physical processes, such as greater SST yielding larger surface heat fluxes. Other variables co-vary because their definitions are linked, such as lower SST occurring with stronger LTS. Some variables with opposing trends on cloud dissipation can be correlated themselves, causing the total cloud response to be dominated by only one variable and masking the independent effect of the non-dominant variable. This is the case for stronger subsidence, which tends to thin Sc clouds, being correlated with larger LTS, which tends to sustain a thicker cloud— their combined occurrence is linked to larger cloudiness due to dominance by LTS (Myers and Norris 2013; Seethala et al. 2015). Such co-variability can arise from seasonal trends, such as decreasing LTS co-occurring with increasing SST, which causes cloudiness to decrease from May/June to August/September in Southern California (Clemesha et al. 2016; Klein and Hartmann 1993).

The research-to-date on coastal Sc dissipation presents several gaps: (i) Only a few parameters have been considered, specifically two in Ghonima et al. (2016), while 9 variables have been studied for marine Sc in Seethala et al. (2015). (ii) The parameters do not resemble realistic conditions. Specifically, Ghonima et al. (2016) parameter values for Bowen ratio and sea-breeze advection were chosen ad-hoc and only for two idealized cases. (iii) As a result of (ii), co-variability effects have been ignored.

In this work, we conduct a comprehensive analysis of how coastal Sc cloud dissipation time depends on initial conditions and boundary forcings, with consideration of co-variability. We use a large set of 15 variables measured or derived from realistic meteorological conditions for Southern California as input to a two-column Mixed-Layer Model (MLM) to predict dissipation time (Section 2.a). The two columns represent ocean and land conditions and allow the modeling of sea-breeze advection over coastal land. Realistic conditions for the MLM are obtained from radiosonde profiles, ground measurements, and NWP models for the 2014 to 2017 summer seasons in Southern California (Section 2.b). In Section 3.a, we review the correlations of the variables in the dataset. We perform two analyses in order to consider the impact of co-variability on the predicted dissipation time (Section 3.b). In the first, coastal Sc evolution is simulated for 195 cloudy days in which the initial conditions and forcing parameters co-vary as in nature. In the second, simulations are performed in which a single forcing parameter is varied around an idealized, composite reference simulation. Because the different parameters co-vary in nature, the sensitivity to changes in a single parameter will differ between the two approaches: changes in one variable are accompanied by changes in other variables sampled from their climatological co-variation. In this paper, “co-variability” refers to the effects of these secondary correlations on changes in the evolution of the cloud and, in particular, on the time of its breakup. In Section 3.c, we quantify and compare the dissipation time trends obtained by the different approaches. Section 4 contains the conclusions. For an easier reading, a nomenclature is included in Appendix A.

2. Methods

a. Mixed-Layer Model framework

The MLM used in this study follows the implementation of Ghonima et al. (2016) (refer to Appendix B for further details). In the MLM, the state of the well-mixed ABL is described by three prognostic equations and several parameterizations. The prognostic equations determine the evolution of the thermodynamic state of the ABL, described by: the ABL thickness or inversion base height z_i, the mean liquid water potential temperature in the ABL θ_l^{BL}, and the mean total water content in the ABL q_t^{BL}. Cloud thickness h depends on these three variables, where the cloud top height is also z_i and the cloud base height depends on θ_l^{BL} and q_t^{BL}. The growth of z_i depends on the balance between the entrainment of upper air and large scale subsidence. Changes in θ_l^{BL} depend on the balance of radiation and turbulent fluxes, while the evolution of q_t^{BL} is only determined by turbulent fluxes (precipitation is not considered). Consequently, changes in h are affected by all these factors. Aside from the governing equations, parameterizations in the MLM allow quantifying radiation, entrainment of upper air, large-scale subsidence, and turbulent fluxes at the surface and top of the ABL.

Since we are interested in cloud dissipation over coastal land, a Eulerian framework is preferred, which introduces advection tendencies in the prognostic equations. To account for this effect, we model the evolution of two columns: one over the ocean and the other over land, as illustrated in Fig. 1. The dominant wind direction in this region is from the ocean to the land, day and night, as a consequence of the North Pacific subtropical high and the continental U.S. thermal low during the summer (Halliwell and Allen 1987). Therefore, advection is considered only for the land column, and the advection terms depend on both ocean and land conditions (Appendix B2).

For this study, we are specifically interested in the effect of different variables on cloud dissipation. We accordingly select relevant meteorological variables used by the equations and parameterizations in the MLM. The variables determine the initial conditions and boundary forcings during the simulation. Initial condition variables include the inversion base height z_i, as well as the ABL values of liquid water potential temperature θ_l^{BL} and total water mixing ratio q_t^{BL}, that determine the initial cloud thickness h. Thermodynamic values above the ABL are also part of the initial input, including values at 3 km ($\theta_l^{3\mathrm{km}}$ and $q_t^{3\mathrm{km}}$) and inversion jumps ($\Delta_i\theta_l$ and $\Delta_i q_t$), which are assumed to occur over an infinitesimally thin layer (Lilly 1968).

The parameters used to determine forcings include large-scale, radiative, and turbulent processes. The large-scale parameters are the ABL large-scale divergence D that determines the subsidence rate at the top of the ABL w_{sub} (Eq. B2), an average wind speed $\overline{u}$ for the advection tendencies (Appendix B2), and sea-level pressure (SLP). The radiation parameterization has shortwave and longwave components (Appendix B4), where the solar irradiance above the cloud SW_i along with the cloud properties will determine the shortwave net radiation flux. For the longwave component, the sky effective radiative temperature T_{sky} represents the longwave radiation gain from the sky above the ABL. Lastly, turbulent fluxes exist both at the surface and the top of the ABL (Appendix B5). Surface fluxes depend on the type of column: for the ocean, we prescribe sensible and latent heat fluxes (SHF and LHF) as daily averages, and for the land, we prescribe a Bowen ratio Bo that partitions the sensible and latent heat fluxes. At the top of the ABL, the turbulent fluxes are determined by the inversion jumps $\Delta_i\theta_l$ and $\Delta_i q_t$ along with the entrainment rate w_e. Lastly, entrainment mixes air from the free troposphere into the ABL through turbulence, which results from a complex combination of radiative cooling, evaporative cooling, and wind shear, among other processes (Mellado 2017). In the MLM, the entrainment parameterization depends on most of the other variables described (Appendix B3). Entrainment acts as a regulating mechanism in response to cloud thickness as it promotes thinning for thicker clouds (Zhu et al. 2005). Entrainment also favors dissipation over land as larger surface fluxes increase w_e and both surface fluxes and entrainment promote ABL heating, thinning the cloud.

A comment on the choice of the data / modeling tool for the analysis is in order. We use a MLM because it allows a comprehensive sensitivity analysis in an idealized geometry. Conversely, real observations would introduce unknowns, uncertainties, and errors. For example, real 3D topography affects dissipation time due to differential heating and differences in boundary layer height, while the MLM allows removing these effects. Another example is that boundary layer heights are only observed twice per day in reality while the MLM provides a detailed evolution. A detailed discussion of the benefits of the MLM framework is provided in Appendix D.

b. Data

To study how different variables influence Sc dissipation time, we created a comprehensive dataset with realistic Sc conditions for the years 2014 to 2017 in Southern California. It is important to consider realistic conditions to understand if the influence of a variable is actually observable / relevant, as well as to understand which variables need to be measured / obtained to improve cloud dissipation predictions. The dataset contains the variables needed in the MLM: inversion height z_i, liquid water potential temperature $\theta_l(z)$ and total water mixing ratio $q_t(z)$ profiles, ABL large-scale divergence D, average wind speed $\overline{u}$, Bowen ratio Bo, incoming solar irradiance above the cloud SW_i, sky effective radiative temperature T_{sky}, SLP, and ocean sensible and latent heat fluxes (SHF and LHF). May through September months are selected as they constitute the Sc cloud season, and also when the highest solar irradiance is available. The variables are obtained from different sources including radiosondes, Numerical Weather Prediction (NWP) model outputs, observations, and radiative models. Further details are provided in Appendix C.

ABL thickness z_i and profiles of liquid water potential temperature $\theta_l(z)$ and total water mixing ratio $q_t(z)$ are processed from radiosonde data to be compatible with the MLM framework (Appendix C2). We analyze early morning radiosondes at the NKX Miramar Marine Corps Air Station in San Diego, CA. First, the inversion base height z_i is detected as the starting point of the largest temperature inversion. Next, we check if the state of the ABL could be decoupled using the criterion $|\theta_{vb} - \theta_{v0}| > 1$ K (Ghate et al. 2015), where θ_{vb} and θ_{v0} are the virtual potential temperature at the radiosonde cloud base (the point where the relative humidity (RH) exceeds 95%) and at the surface, respectively. Decoupled cases are discarded because the MLM cannot describe the ABL physics appropriately. For the remaining cloudy cases, the state of the ABL is averaged to create a well-mixed profile described by θ_l^{BL} and q_t^{BL}. Lastly, the free troposphere is included by considering data above the inversion region up to 3 km. While moisture above the inversion is assumed to be constant and represented by an average value of total water mixing ratio $q_t^{3\mathrm{km}}$ and a sharp inversion jump of total water mixing ratio $\Delta_i q_t$, the liquid water potential temperature is fitted into a linear profile and represented by the value of the fit at 3 km $\theta_l^{3\mathrm{km}}$ and by the sharp inversion jump $\Delta_i \theta_l$. Fig. 2 shows an example of the processed well-mixed ABL structure. Since the initial state is derived from the radiosonde launched at 0300 LST (11 UTC), we use that time to initialize the simulations. Furthermore, we assume that this early state is representative of both ocean and coastal land and thus, start the MLM with the same initial condition for both columns. This assumption is justified as the region experiences a sea breeze day and night and night time surface radiative cooling over land is small due to the Sc cloud cover.

The radiation model in the MLM depends on SW_i for the shortwave and T_{sky} for the longwave radiation fluxes. For obtaining SW_i, we assume that there are no other cloud layers overhead– typical for the summer season in Southern California (Christensen et al. 2013)– and calculate the daily maximum of global horizontal irradiance (GHI) from a clear sky model (Ineichen and

Perez 2002). For obtaining T_{sky}, we solve for the longwave radiative fluxes across the whole atmosphere by inputting the temperature profiles from the radiosonde into the Streamer radiative transfer model (Key and Schweiger 1998) and calculating T_{sky} as the blackbody temperature from the longwave downwelling flux at the top of the cloud (Appendix C3).

We estimate $\overline{u}$ and SLP from measurements at the NKX METAR weather station. We compute $\overline{u}$ as the average of the westerly wind speeds between 0500 and 2100 LST and scale a 10-year average daily profile to recreate the diurnal cycle (see Fig. B1-b). This daily profile never reaches zero, so advection is continually present during the day (Appendix C5). We compute SLP as a daily average.

For the turbulent fluxes at the surface, we take different approaches for the ocean and land columns. For the ocean column, the prescribed values of sensible and latent heat surface fluxes (SHF and LHF) are computed with a bulk formula (Appendix C5) from observations of wind speed $\overline{u}$ and daily averages of sea surface temperature (SST) at the Torrey Pines Outer station obtained from the National Data Buoy Center (NDBC) (NOAA 2017). For the land column, we estimate a daily Bowen ratio Bo at NKX by analyzing in-house operational runs of the Weather Research and Forecasting (WRF) model. Bo is computed as the ratio between SHF and LHF at the nearest grid point to the NKX station, averaged between 0800 and 1500 LST (Appendix C4).

Lastly, we estimate large-scale divergence D from the North American Mesoscale Forecasting System (NAM) as the partial derivative of pressure vertical velocity ω with respect to pressure in the ABL (Appendix C4).

c. *Steady thickness initialization (STI)*

The MLM is initialized at 0300 LST prior to sunrise, when we expect a stable Sc behavior. Nevertheless, we occasionally observed large changes in modeled cloud thickness in the first few hours after initialization but still prior to sunrise, indicating possible inconsistencies in the initial state. For reference, Duynkerke et al. (2004, Fig. 4) observed ΔLWP$/\Delta$t tendencies of 2.8 g m^{-2} h^{-1} and 7.6 g m^{-2} h^{-1} at 0300-0400 LST. In contrast, the first-hour average of ΔLWP$/\Delta$t for our preliminary MLM runs ranged between -42 g m^{-2} h^{-1} and 12 g m^{-2} h^{-1}.

The reasons for large model tendencies following initialization are multifold: (i) The well-mixed approach fits the radiosonde data to a slightly different state (Fig. 2); (ii) radiosonde measurement errors, especially in the humidity measurement; (iii) LWP is not measured and has to be derived using a crude model ($\mathrm{LWP} = \int_0^{z_i} \rho(z) q_l(z) dz$, where $\rho(z)$ is the density of air); (iv) the MLM does not adequately describe all ABL physics; and (v) uncertainties in the estimated large-scale divergence. Since the variable inter-dependencies will be studied as a function of the initial conditions, it is important that the initial conditions are representative of the first few hours of the simulations. While initial variables should reflect real conditions as much as possible, our main objective is to understand the sensitivities of Sc evolution. Therefore, a stable, self-consistent MLM initialization is the priority and slight deviation from measured conditions when needed is tolerated. The steady thickness initialization (STI) method was developed to create a stable initial condition from the measured profiles.

We seek a more stable state by keeping z_i constant and varying the set of thermodynamic variables $\mathbf{s} \equiv (\theta_l^{\mathrm{BL}}, \Delta_i \theta_l, q_t^{\mathrm{BL}}, \Delta_i q_t)$. For mathematical consistency, the tropospheric mixing ratio $q_t^{3\mathrm{km}}$ will also be modified (since it is the sum of ABL and inversion jump quantities). We do not seek a state with zero tendency because (i) we want to avoid deviating too much from the original state, (ii) there is no unique value of $\mathbf{s}$ that satisfies the steady thickness condition (van der Dussen et al. 2013, Fig. 3), and (iii) it has been observed that the z_i tendencies at dawn are small but not zero. Instead, we seek for a close, more stable state $\mathbf{s}$ by thresholding the rate of change of thickness

(Eq. 1).

$$\left|\frac{\partial h}{\partial t}\right| = \left|\frac{\partial z_i}{\partial t} - \frac{\partial z_b}{\partial t}\right| < 5 \cdot 10^{-3}\ [\mathrm{m\ s^{-1}}] \tag{1}$$

Using an iterative gradient descent method the 4 variables change at the same time (Eq. 2), in an amount proportional to the local gradient of the thickness tendency.

$$\mathbf{s}_{n+1} = \mathbf{s}_n - \mathrm{sgn}\left(\frac{\partial h}{\partial t}(\mathbf{s}_n)\right) \xi \nabla \frac{\partial h}{\partial t}(\mathbf{s}_n), \tag{2}$$

where ξ is the proportionality constant used to follow the gradient; $\xi = 0.1$ yielded satisfactory results for most days. We compute the gradient with second order central finite differences using a step of 0.1 K or 0.1 g kg^{-1} in each component of $\mathbf{s}$ and iterate until the thinning or thickening is less than 5 mm s^{-1} (Eq. 1). An example of the effect of the STI is shown in Fig. 3. The strong thinning experienced in the first hour of simulation with the original initial conditions is greatly reduced, and the STI initial conditions yield -6.4 g m^{-2} h^{-1} $< \Delta\mathrm{LWP}/\Delta\mathrm{t} <$ 12 g m^{-2} h^{-1}, in better agreement with observations in Duynkerke et al. (2004, Fig. 4).

Finally, we remove STI states that lie far from the original using a squared distance threshold

$$d^2 = \sum_{i=1}^{4}\left(\frac{s_i^{\mathrm{STI}} - s_i}{s_i}\right)^2 = 0.005,$$

where s_i and s_i^{STI} are the components of $\mathbf{s}$ prior and after the STI method is applied, respectively. Twelve cases are removed in this way. For the final set of 195 cases used in the analysis, 115 cases were not modified by the STI, as the original state was already steadier than 5 mm s^{-1}, and for the 80 cases that were modified, the average d^2 was 0.0007.

d. Model runs

The STI-adjusted dataset becomes the new input to the MLM. The initial conditions are the STI thermodynamic profiles derived from the radiosonde. The other variables are related to forcings at the boundaries of the ABL, such as air mass advection and fluxes at the surface and inversion levels. The MLM predicts the evolution of the cloud and yields the cloud dissipation time over land. Simulations are terminated when clouds dissipate because the increase in solar heating of the ABL prevents cloud reformation until evening and because several model assumptions (e.g. the entrainment calculation) are no longer valid.

e. Data subsetting

Some of the original 278 cloudy and not decoupled days produced results inconsistent with the MLM assumptions: (i) STI leading to a cloudless state; (ii) negative entrainment values that may be related to decoupling (Appendix B3); (iii) clouds whose base reached the surface during the simulation (the longwave radiation scheme in the MLM may not represent fog conditions accurately); (iv) otherwise extremely thick clouds that could precipitate (precipitation is not modeled in the MLM), using a threshold of LWP $= 250$ g m^{-2}; and (v) days with precipitation at the METAR station. After filtering these cases out, we were left with a dataset of 195 days.

f. Sensitivity analyses

1) ALL VARIABLES CO-VARY ON 195 REAL DAYS

We analyze the results of the MLM runs for the diverse conditions of 195 days that span a broad range of the parameter space and display co-variability. We investigate the trends in dissipation time over land, t_{diss}, in relationship to each one of the variables of interest.

2) SINGLE VARIABLE CHANGES FROM A REFERENCE CASE

The results of the cases with co-variability can be difficult to analyze, as different impacts can be enhanced or diminished by the combination of different variables. To aid the understanding of the co-variability analysis, we first identify the individual influence of each variable on dissipation time through a traditional sensitivity analysis. We vary one variable at a time from an idealized reference case composed of the medians of all the MLM input variables: z_i, q_t^{BL}, $\Delta_i q_t$, $q_t^{3\mathrm{km}}$, θ_l^{BL}, $\Delta_i\theta_l$, $\theta_l^{3\mathrm{km}}$, $\bar{u}$, SW_i, D, Bo, SLP, T_{sky}, SHF, and LHF. The purpose of using this idealized reference case is to be able to change most variables in their observed ranges. A set of 5 equidistant points between the percentiles p_{25} and p_{75} of the observed distribution for that input variable is simulated.

The other 14 variables are held constant with the following exceptions: (i) $\Delta_i q_t$ and the tropospheric mixing ratio are varied together for self-consistency (Eq. C3); (ii) z_i is varied following two approaches: (ii-a) variations of z_i alone, which yields different cloud thicknesses, and (ii-b) variations of z_i with constant cloud thickness obtained by adjusting q_t^{BL}; (iii) variations of cloud thickness h with constant z_i and θ_l^{BL} obtained by adjusting q_t^{BL}.

The motivation for (ii-b) is to assess the changes of z_i without the feedbacks related to the abrupt change in cloud thickness. We refer to (ii-b) as varying $z_i|_h$, and we calculate the adjusted $q_t^{\mathrm{BL}}(z_i|_h)$ using $\partial z_b/\partial q_t^{\mathrm{BL}}$ (Ghonima et al. 2015, Eq. 15) (Eq. 3).

$$(q_t^{BL})_{new} = (q_t^{BL})_{old} + \Delta z_i \frac{\partial q_t}{\partial z_b} = (q_t^{BL})_{old}\left(1 + \frac{g}{R_d T_b}\left(1 - \frac{L_{lv} R_d}{C_p R_v T_b}\right)\Delta z_b\right), \tag{3}$$

where $(q_t^{\mathrm{BL}})_{new}$ is the value of moisture needed for the updated height $(z_i)_{new}$ with respect to the original $(q_t^{\mathrm{BL}})_{old}$. For varying $z_i|_h$, h is constant and $\Delta z_b = \Delta z_i = (z_i)_{new} - (z_i)_{old}$ is the change in cloud thickness from the reference case, with $(z_i)_{old}$ the reference case inversion base height. T_b is the temperature at the original cloud-base height.

Similarly, the motivation for (iii) is to assess the changes of h without the effects of varying z_i. We refer to this case as varying $h|_{z_i}$, and the adjusted $q_t^{\mathrm{BL}}(h|_{z_i})$ is obtained with Eq. 3, taking $\Delta z_b = -\Delta h = (h)_{old} - (h)_{new}$ because z_i is constant. Here, $(h)_{old}$ is the cloud thickness for the reference case and $(h)_{new}$ is the updated cloud thickness.

3. Results and discussion

a. Data statistics and correlations

We present a description of the most important inter-correlations within the dataset, which is crucial for understanding the results of the impacts when all variables co-vary. Table 1 shows the main statistics, including diagnostic variables from the MLM (cloud-base height z_b, cloud thickness h, inversion jump of virtual potential temperature $\Delta_i \theta_v$, and liquid water path LWP) and for the well-mixed profiles before and after STI. In the remainder of this section, we describe the main correlations (Fig. 4), distinguished by the nature of their relationship (seasonal trends, initial conditions, and boundary forcings). We emphasize that initial conditions are prior to sunrise and represent both coastal land and ocean conditions.

Given the large number of variables, Principal Component Analysis (PCA) would seem to be a relevant tool. We do not report PCA results for this dataset because the reduction of dimensions is limited (it takes 10 variables to explain 90% of the variance) and the resulting parameter space is non-physical.

1) Variables affected by seasonal trends

Our dataset includes measurements taken between May and September, a time span that is long enough to show seasonal patterns that influence the correlation between some variables (no de-trending is performed in this dataset). While solar irradiance above the cloud SW_i varies during the year, peaking on June 21, the set of temperature variables SST, θ_l^{BL}, and T_{sky} peak in early August. The time lag between SW_i and the temperature variables is influenced by the seasonal pattern of SST, which in turn is affected by the oceanic upwelling that is stronger during June and July for Southern California (Clemesha et al. 2016) as well as the thermal inertia of the ocean. The time lag is long enough to cause a negative correlation between temperatures and SW_i as shown in Fig. 4-a.

The strong correlation between SST and θ_l^{BL} results from the strong influence of ocean SST on the early morning coastal air temperature through horizontal advection.

2) Variables that determine initial conditions

The initial state, prior to sunrise, comprises z_i, $q_t(z)$, and $\theta_l(z)$, which together determine h. By definition, a warmer ABL that is cloudy is at (in-cloud) or near (below-cloud) saturation and can contain more water due to the Clausius-Clapeyron relationship; this makes θ_l^{BL} and q_t^{BL} highly correlated. Conversely, conditions that are warm and dry (causing a negative correlation) are less likely to sustain a cloud and are therefore under-represented in the dataset.

Inversion base height z_i is strongly anticorrelated with q_t^{BL}; a deeper ABL is associated with lower temperature at the inversion base, requiring less water content to be present to saturate and form a cloud. Entrainment also supports this relationship, as prolonged or stronger entrainment can result in deeper ABLs and a lower q_t^{BL}. Interestingly, the relationship between the primary 3 ABL variables $q_t^{\mathrm{BL}}, z_i, \theta_l^{\mathrm{BL}}$ is observed to be linear (R^2 of linear fit is 0.945, Fig. 7-a) and closely follows saturation conditions (see Appendix E). Although a linear relationship exists, only two of the three pairs are correlated, as z_i and θ_l^{BL} do not correlate; therefore, q_t^{BL} acts like a dependent variable.

Cloud thickness h is defined as the difference between cloud-top z_i and cloud-base z_b heights. One might expect lower cloud base to mean greater cloud thickness, but instead variations in cloud thickness are dominated by variations in ABL top height (deeper ABLs have more room for thick clouds). The correlation between z_i and q_t^{BL} causes thicker clouds to be strongly associated with smaller q_t^{BL}. Cloud thickness is also strongly correlated with $\Delta_i\theta_l$ because a stronger temperature inversion limits the entrainment of drier and warmer air into the ABL, which thins the cloud. Fig.4-b shows that both z_i and $\Delta_i\theta_l$ influence h. Although the linear correlation coefficient is only 0.61, both variables combined explain nearly all the variance in h: ABLs with lower (higher) tops and weaker (stronger) capping inversions are related to thinner (thicker) clouds. Note that $\Delta_i\theta_l$ and z_i are not correlated in our dataset (Fig. 4). While this may seem counter-intuitive as strong LTS has been linked to shallower ABLs (Klein and Hartmann 1993), LTS not only depends on $\Delta_i\theta_l$ but also on z_i. Following Wood and Bretherton (2006), the correlation coefficients of z_i and $\Delta_i\theta_l$ with LTS are -0.48 and 0.84, respectively.

For the tropospheric quantities, $q_t^{3\text{km}}$ correlates with q_t^{BL}: a smaller q_t in the ABL is related to a smaller q_t above. The same logic explains the correlation between $\theta_l^{3\text{km}}$ and θ_l^{BL}.

3) Variables that determine boundary forcings

Here, correlations between parameters that specify the boundary forcing of the ABL from above and below are described. Large-scale subsidence, represented by the horizontal divergence D, is weakly correlated with z_i even though subsidence pushes the ABL top down. At -0.08, the correlation coefficient is small, which could be related to errors in estimating divergence, or to the different values of entrainment that also affect z_i, or due to time lags / phase shifts between when changes in D affect z_i, thus weakening the correlation between the two variables. From Myers and Norris (2013), we would expect subsidence to also influence $\Delta_i\theta_l$, but the correlation between D and $\Delta_i\theta_l$ is weak. This disagreement may be explained also by the variables being out of phase and by the exclusive use of well-mixed Sc-capped ABLs in our dataset (versus all ABLs in Myers and Norris (2013)), since other ABL types tend to be associated with smaller D and smaller $\Delta_i\theta_l$.

Surface fluxes affect both temperature and moisture in the ABL. Over the ocean, LHF and SHF correlate with $\overline{u}$ by definition (Eqs. C8, C9). LHF is correlated with z_i while SHF is not. A larger

LHF was also related to a larger z_i in (Bretherton and Wyant 1997) probably because a larger LHF is related to a smaller q_t^{BL} (by definition), which in turn correlates to a larger z_i. In contrast, SHF depends on θ_l^{BL}, which is not correlated to z_i.

Over land, Bo is negatively correlated to q_t^{BL} as an ABL with stronger surface latent heat fluxes causes both a larger q_t^{BL} and a smaller Bo. Secondary variable correlations (q_t^{BL} to θ_l^{BL} and z_i) explain the correlation of Bo to θ_l^{BL} and z_i.

The last set of forcings are the radiative fluxes. For the shortwave portion, the yearly variations of solar irradiance causes SW_i to be anti-correlated with temperature metrics (Section 3.a.1). For the longwave portion, T_{sky} is correlated with q_t^{3km} due to the longwave absorption and emission by water molecules above the cloud (Fig. B1-a). Secondary variable correlations (q_t^{3km} to q_t^{BL} and z_i) explain the correlation of T_{sky} with q_t^{BL} and z_i.

b. Dissipation time dependence

We now review the results of the sensitivity analyses of modeled dissipation time, defined as the time when cloud thickness h becomes zero. The main focus of this section is to compare the co-variability results of the 195 simulated days to the single variable changes as well as previous studies. The discussion is subdivided into initial conditions and forcing parameters.

The co-variability results for the 195 MLM simulations are shown in Fig. 5. The t_{diss} histogram (Fig. 5-a) shows that clouds either dissipate before 1300 LST or persist for the whole day. We refer to these two categories as dissipating and persisting cases, respectively, so t_{diss} is defined for dissipating clouds only. Some of the variables influence t_{diss}, while others differ markedly between dissipating and persisting cases, and some show unclear trends or non-monotonic tendencies. Figs. 5-b-r show the top 17 trends with linear fits for t_{diss} with $\mathrm{R}^2 > 0.02$ or with a noticeable difference between persisting and dissipating cases. Dissipation time is strongly related to h, z_i, LWP, q_t^{BL}, $\Delta_i\theta_l$, T_{sky}, and oceanic SHF; while $\overline{u}$, Bo, and D show weaker trends.

The results for the single variable changes from an idealized reference case while holding all other variables constant are shown in Fig. 6, where simulated dissipation time for the land column is plotted against the variables' Z-score (subtracting observed mean and dividing by the standard deviation) for ease of comparison. The idealized reference case corresponds to a coastal cloud that dissipates around 0800 LST (continuous line in Fig. F1).

1) Initial ABL state

The initial state of the ABL affects the dissipation time more than the forcing parameters. The components of the initial state are z_i, q_t^{BL}, and θ_l^{BL}, which have an intricate relationship (Section 3.a.2), and together determine h. Although h is not an explicit input variable to the MLM, we include it in the analysis because of its strong trend, the fact that it is readily observable, and its importance for entrainment and radiation.

For all the approaches considered, h has the most robust relationship with t_{diss}, followed by z_i. Thicker clouds or deeper ABLs either dissipate later or persist for the whole day. Similarly to marine Sc (Burleyson and Yuter 2015), clouds that are thicker at dawn can withstand more solar heating and delay dissipation. For both h and z_i, co-variability weakens the single variable changes trends on t_{diss} (Figs. 5-e,b and 6-a) because the independent effects are diminished by the effects of the variables that co-vary with them, such as q_t^{BL}. For z_i, the co-variability trend is more similar to the experiment where cloud thickness is held constant by varying $z_i|_h$ together with q_t^{BL} (Fig. 6-b). This means that even when we control for the strong effects of h, other variables with weaker independent trends also impact the final trend for z_i. The trends for h and z_i imply a strong trend for LWP as well (Fig. 5-q). Since z_i and h are correlated, we analyze the trend of t_{diss} with respect to both variables. Fig. 8-b shows that dissipation time varies with both h and z_i, but it is more strongly correlated with cloud thickness.

While colder ABLs are related to later dissipation, as expected, moister ABLs dissipate earlier with co-variability. For θ_l^{BL}, the trend with co-variability (Fig. 5-c) is weaker than for the single variable changes (Fig. 6-a), and for q_t^{BL}, the trend with co-variability (Fig. 5-d) is completely opposite to the single variable changes (Fig. 6-a). This seeming contradiction is actually in agreement with the strong correlations observed between larger q_t^{BL} and both lower h and z_i and larger θ_l^{BL}, which shorten cloud lifetime.

The fact that q_t^{BL} does not dominate the trend with co-variability also agrees with the linear dependence of q_t^{BL} on z_i and θ_l^{BL} (Section 3.a.2), and with the cloud thickness regulation feedback. Cloud thickness is regulated towards an equilibrium state in that thicker clouds enhance cloud radiative cooling and entrainment, which in turn thin the cloud and regulate h (Zhu et al. 2005). At nighttime, thinner clouds will experience weaker entrainment due to the regulating feedback, keeping the ABL moister and shallower and supporting the negative correlation between z_i and q_t^{BL}, and between h and q_t^{BL}. For these initially thin clouds experiencing reduced entrainment, we expect a shorter cloud lifetime, which agrees with the trend of weaker first hour initial entrainment rates $\overline{w_{e,1h}}$ and earlier t_{diss} (Fig. 5-p). Lastly, Fig. 8-a visually shows the lack of dominance of q_t^{BL} on t_{diss} when compared to z_i: the gradient of dissipation time, as well as the region of persisting clouds, are more strongly correlated with z_i than q_t^{BL}, meaning that the trend between q_t^{BL} and t_{diss} in Fig. 5-d is a consequence of the anti-correlation between z_i and q_t^{BL}.

2) Inversion jumps and free-tropospheric conditions

While the inversion jumps and free-tropospheric state are part of the initial conditions, we analyze them separately because they represent the interaction between the ABL and free troposphere, rather than the ABL state. Stronger temperature inversion jumps $\Delta_i\theta_l$ and weaker moisture inversion jumps $\Delta_i q_t$ (moister tropospheres) delay dissipation time (Figs. 5-f,g), in agreement with most previous studies.

The effect of stronger temperature inversion jumps $\Delta_i\theta_l$ agrees with the result for the single variable changes (Fig. 6-a) for our reference case. Ma et al. (2018) obtained a $\Delta_i\theta_l$ trend that opposed ours and that of Xu and Xue (2015), and argued that the impacts of the temperature inversion jump might depend on the reference case selected. There are competing effects of $\Delta_i\theta_l$: while a stronger temperature inversion jump reduces the entrainment rate, it also means that the entrained air is warmer. Mathematically, the net warming heat flux is the product of a reduced entrainment rate and a stronger inversion jump, and the direction of the effect for the product could vary for different conditions (Eq. B15). For our reference case, the diminished entrainment rate dominates the over the warmer entrained air, delaying the dissipation by maintaining the ABL moister and colder over land and ocean (Fig. F1-a). Our results with co-variability support the trend of Xu and Xue (2015) and van der Dussen et al. (2015), as well as the trend of increased cloudiness with stronger $\Delta_i\theta_l$ in previous climate studies (Seethala et al. 2015; Klein and Hartmann 1993; Klein et al. 1995; Wood and Bretherton 2006). Nonetheless, we note that persisting clouds do not predominantly exhibit stronger inversion jumps.

As was the case with h, the influence of $\Delta_i\theta_l$ on t_{diss} is not dominated by z_i. This is evident in the two-dimensional space of z_i jointly with $\Delta_i\theta_l$. Fig. 8-c shows that earlier dissipation (persisting clouds) occurs for shallow (deeper) ABLs under a weak (strong) inversion, which also corresponds to the conditions for thinner clouds shown in Fig. 4-b.

For moisture, weaker inversion jumps $\Delta_i q_t$ (relatively moister free tropospheres) are linked to persisting clouds, although dissipation time (as a continuous variable) is not strongly correlated to $\Delta_i q_t$ (Fig. 5-g). The trend is consistent with the single variations due to reduced entrainment drying (Fig. 6-a), in agreement with the LWP responses reported by van der Dussen et al. (2015); Xu and Xue (2015); Ma et al. (2018).

At first glance, the co-variability trends of $\Delta_i q_t$ and $q_t^{3\mathrm{km}}$ seem contradicting: weaker $\Delta_i q_t$ (relatively moister free tropospheres) and also lower $q_t^{3\mathrm{km}}$ (drier free tropospheres) lead to persisting clouds (Figs. 5-g,h). However, a weaker $\Delta_i q_t$ is only a free troposphere that is similar in moisture to the ABL, and not necessarily a moister free troposphere. Thus, a very dry free troposphere can have a weak inversion jump if the ABL is also dry. Nevertheless, the trend of a dry troposphere extending dissipation time is still unexpected since it opposes the single variable changes (Fig. 6-a). The strong correlations between drier $q_t^{3\mathrm{km}}$ to higher z_i and lower T_{sky}, both of which extend cloud lifetime, explain the trend. Previous studies have related moister free tropospheres to reduced cloudiness (Dal Gesso et al. 2014; Seethala et al. 2015), where the latter (correctly) speculated that correlations rather than physical processes are responsible for the trend.

The combined effects of moisture and temperature inversion jumps have been studied for the CTEI (Cloud Top Entrainment Instability), a process that can trigger cloud dissipation (Deardorff 1980; Kuo and Schubert 1988; van der Dussen et al. 2013; Xu and Xue 2015). Even though the stability parameter criterion $\kappa \geq 0.23$ van der Dussen et al. (2013, Eq. 1) was found to be insufficient to predict the CTEI, Fig. 5-r shows a trend between larger κ and earlier dissipation, suggesting that CTEI could be contributing to cloud dissipation for larger κ. Nevertheless, the great dispersion precludes us from stating this conclusively ($\mathrm{R}^2 = 0.03$).

Similarly to $q_t^{3\mathrm{km}}$, $\theta_l^{3\mathrm{km}}$ has a stronger effect with co-variability than in the single variable changes (Figs. 5-i and 6-a). The enhanced effect of $\theta_l^{3\mathrm{km}}$ can be explained by the strong correlation to θ_l^{BL}.

3) SEABREEZE ADVECTION

Since seabreeze advection is crucial in extending the lifetime of coastal Sc (Ghonima et al. 2016), a robust trend between $\overline{u}$ and t_{diss} is expected, as shown by the single variable changes (Fig. 6-c). In actuality, the trends with co-variability show $\overline{u}$ exhibiting a nonlinear behavior where larger wind speeds are associated with both persisting clouds and early dissipation time (Fig. 5-j).

The nonlinear trend of $\overline{u}$ is not related to the physics, but it is caused by a sampling issue. In order to explain this misleading trend, we look at the influence of initial cloud thickness on the relationship between $\overline{u}$ and t_{diss}. Fig. 8-d shows first that h dominates the dependence of dissipation time in the $\overline{u}$ and h space. Second, separating analyses for thick ($h > 150$ m) and thin clouds is enlightening. Thicker clouds persist with larger $\overline{u}$, as expected, and the critical wind speed for clouds to persist decreases with greater initial cloud thickness. For thinner clouds, the dissipation time is not affected by $\overline{u}$. Since the persisting clouds are not part of the trend lines in Fig. 7, a misleading anti-correlation of wind speed and dissipation time is observed. This analysis suggests that advection is irrelevant for thin clouds as they already dissipate before the onset of advection around 0700 LST. Advection does play an important role for thicker clouds that survive through the weak advection period, which then benefit from the cooling associated with stronger advection. This effect was not observed by Ghonima et al. (2016) as they only analyzed two reference cases with the presence or absence of seabreeze.

Another aspect that could cause our results to deviate from real observations is the wind speed input for the MLM. For ease of comparison, we have assumed that the wind speed for all 195 days has the same diurnal variation (i.e., the onset of seabreeze is fixed, but the magnitude changes). However, we speculate that the timing of the sea-breeze onset may be as or more important than the wind speed magnitude. By 0800 LST, when the wind speed increases in our simulation (Fig. C1-

b), 116 days are already clear or have clouds that are already so thin that the heat input from solar radiation dominates over cooling from horizontal advection. For these early morning dissipation cases, the wind speed is irrelevant. This timing dependence was also mentioned by Burleyson and Yuter (2015) for marine Sc, as cloud breakup rates strengthen near noon.

4) SURFACE FLUXES

For coastal Sc clouds, both the surface fluxes over the ocean and over land can affect the cloud evolution. A larger SHF over the ocean is linked to earlier dissipation time, agreeing with previous studies for marine Sc (McMichael et al. 2019; Chlond and Wolkau 2000). The effect of SHF under co-variability is greater than for the single variable changes (Figs. 5-k and 6-c). In contrast, the influence of LHF on t_{diss} is weak with co-variability, despite the existence of persistent clouds for larger LHF (Fig. 5-l) supporting the trend of the single variable changes (Figs. 6-c). This difference between the effect of SHF and LHF suggests that the importance of the ocean fluxes, which influences coastal clouds through advection, may be greater for temperature than for moisture, agreeing with Ghonima et al. (2016).

Over land, the influence of Bo on dissipation time does not show a strong trend when co-variability is considered, but persistent cases are related to higher Bo (Fig. 5-m), contradicting Ghonima et al. (2016) and the trends of single variable changes. This unexpected effect is a consequence of the correlation between Bo and q_t^{BL}.

5) LARGE-SCALE FORCINGS

Subsidence is known to be of great importance for the evolution of Sc clouds. Stronger D reduces cloud lifetime by thinning the cloud from the top, and the clouds that persist have lower D (Fig. 5-n), agreeing with the single variable changes (Fig. 6-d), as well as the response in LWP in previous sensitivity studies (McMichael et al. 2019; Ma et al. 2018; van der Dussen et al. 2016; Noda et al. 2014; Blossey et al. 2013) and the response in cloudiness for independent changes of subsidence (Myers and Norris 2013).

Aside from subsidence, SLP is an indicator of the synoptic conditions over the coast of California. Although there is not a robust impact of SLP on t_{diss} with co-variability (not shown), we note that the physical impact of a smaller SLP yields later t_{diss} because –for constant θ_l^{BL}– a colder temperature profile is needed to balance the change in pressure, resulting in a thicker cloud.

6) Radiative forcings

We have two radiation parameters of importance for dissipation of coastal clouds representing radiative cooling and solar heating. Stronger radiative cooling, represented by a lower T_{sky}, delays dissipation with the most robust trend of all the forcing parameters (Fig. 5-o). This effect agrees with the single variable changes (Fig. 6-d) and previous studies (Kopec et al. 2016; Chlond and Wolkau 2000).

For the solar heating, $\mathrm{SW_i}$ shows no clear trend with t_{diss} under co-variability (not shown). Meanwhile, the effect observed for single variable changes is that increased heating shortens cloud lifetime (Fig. 6-d), as the additional heating of the cloud and the land surface accelerates dissipation. Although SW_i was found to strongly influence the rate of cloud breakup for marine clouds (Burleyson and Yuter 2015), that effect may be reduced by the dominance of other factors such as ABL depth and cloud thickness.

c. Summary, quantification, and discussion of dissipation trends

Most of the impacts of different variables on cloud dissipation time over land were either diminished or increased when considering co-variability, while others were unexpected due to the correlations among parameters related to forcings and initial conditions. In this section, we summarize and quantify the most robust trends when all variables co-vary and compare them to the trends resulting from changes in a single variable when all others are held constant.

The trends are expressed as $\delta\psi/\delta t_{diss}$, quantifying how much change in a variable ψ is needed to delay t_{diss} by one hour. Thus, the greater the number, the less sensitive t_{diss} is for that variable. For the analysis of changes with all variables co-varying, we obtain one-dimensional linear fits for all dissipating cases. For the analysis of changes in a single variable from a reference case with all other variables held constant, we calculate the slope $\delta\psi/\delta t_{diss}$ also for all dissipating cases. We also compute trends for the two-dimensional space spanned by strongly correlated variables z_i and q_t^{BL} as a two-dimensional linear fit of all the points to estimate the relationship between t_{diss} and the two variables (z_i, q_t^{BL}) as

$$\Delta t_{diss} \approx \frac{\delta t_{diss}}{\delta z_i}\Delta z_i + \frac{\delta t_{diss}}{\delta q_t^{\mathrm{BL}}}\Delta q_t^{\mathrm{BL}}. \tag{4}$$

The results of the different methods are shown in Table 2. We acknowledge that for the single variable changes the linear trend results depend on the reference case and only a single reference case is considered here. For the dissipation time trends when all variables co-vary, the different linear fits are also an approximation since the behavior is likely to be nonlinear based on the non-linearities in the entrainment and radiation parameterizations. The estimated trends should be interpreted with caution, as they are marginal views of the behavior in the multi-dimensional space and other variables will naturally vary and contribute to the overall impact.

The most consistent trend is the $\delta\psi/\delta t_{diss}$ response to changes in z_i. A greater change of z_i is needed to influence t_{diss} when all variables co-vary (163.9 m h^{-1}) compared to when only z_i varies and other variables are held constant (50.40 m h^{-1}). The $\delta\psi/\delta t_{diss}$ response is least sensitive for changes in inversion base height with cloud thickness held constant ($z_i|_h$, 320.9 m h^{-1}) probably because the z_i change is not reinforced by changes in initial h. For h, we find a similar effect of co-variability, requiring greater changes (319.6 m h^{-1}) compared to when only $h|_{z_i}$ was varied (78.74 m h^{-1}).

The impact of q_t^{BL} on t_{diss} is strong, but the different approaches yield contradictory trends, as discussed in Section 3.b.1. While the single variable changes yielded a positive $\delta\psi/\delta t_{diss}$ response (0.359 g kg^{-1} h^{-1}), the fit for q_t^{BL} when all variables co-vary (-2.826 g kg^{-1} h^{-1}) and the fit in the 2D (q_t^{BL},z_i) space (-21.11 g kg^{-1} h^{-1}) are both negative. Meanwhile, the constant cloud thickness analysis varying $z_i|_h$ yields a similar value to the trend with co-variability (-1.891 g kg^{-1} h^{-1}).

The comparison of the sensitivity of dissipation time when a single variable changes to sensitivity when all variables co-vary highlights the difficulty in finding universal cloud response trends because of the multi-dimensionality and inter-correlations in the dataset. Changing a single variable ignores its correlations with other variables and may create unrealistic meteorological conditions. Simplified co-variability, such as variations of $z_i|_h$ together with q_t^{BL} to minimize feedbacks related to strong changes of cloud thickness, can yield more realistic trends. However, we are not able to isolate the unique influence of one variable on dissipation time when all variables co-vary, and the net effects are composed of all the correlated variable contributions. However, the trends in cloud dissipation time when all variables co-vary can quantify the marginal impact of a variable in the most realistic way, in the sense that it is what we would observe in nature if we were to measure a limited number of variables. Still, co-variability effects are found to be too important to ignore, and thus, they should be considered in sensitivity analyses in order to improve prediction models.

The timing of dissipation may also affect the importance of some variables, as noted by Burleyson and Yuter (2015) in explaining why breakup rates of marine Sc are stronger in the late morning. Over coastal land, when t_{diss} is closer to noon, wind speed and solar irradiance are greater than in the early morning and the same relative change in these variables would cause a larger absolute change in advective cooling and solar heating. This dependence on dissipation timing could apply to all variables with diurnal cycles, such as $\overline{u}$, Bo (as it is applied to surface fluxes over land), and $\mathrm{SW_i}$. In fact, Figs. 5-j-o show that most cases resulting in early dissipation times are caused by a larger range of forcing variables than later dissipation times. Because of this spread in the early morning cases, the dissipation trends can be affected. Elucidating the extent of this impact is left for future work and it can indeed help to move forward to more realistic predictions.

While the physical processes described are consistent with the statistical results in this paper, simplifications may affect real dissipation trends: (1) The wind speed timeseries was simplified to allow a more standardized comparison. (2) Uncertainties exist in the estimation of D and Bo. (3) The ABL is assumed to be well-mixed. (4) Decoupling is not considered in the MLM, which might influence the real trends related to z_i and dissipation time even though cases that were initially decoupled were removed from the analysis. Even though this means that the prediction skill of the model is currently not sufficient to predict real dissipation times (as discussed in Appendix D), it also means that the complex results obtained are a pure consequence of the co-variability within the dataset. If co-variability has such a great influence on the results of a simple model such as the MLM, it will probably have it to a greater extent in more complex models and in nature.

4. Conclusions

We have studied the effects of several variables on the predicted dissipation time of Sc clouds over a coastal region using a realistic dataset and a two column Mixed-Layer Model. The dataset included 195 Sc days in the summers of 2014 to 2017 in Southern California, with 15 variables acting as initial and forcing parameters in the MLM.

The main findings are summarized as follows:

- This work confirmed the importance of initial ABL height and cloud thickness in coastal Sc dissipation, in agreement with the trends of cloudiness for marine Sc. If these two variables could be measured more accurately and time-resolved in coastal areas using lidar, solar forecasts in the area could be improved.

- Co-variability results, in which perturbations to one variable are accompanied by correlated variations in other variables related to initial conditions and forcings from a sample of 195 cloudy days, differ greatly from a traditional, single-variable sensitivity analysis. In most cases, co-variability only strengthened or diminished the trend of a variable (albeit sometimes substantially), while in other cases the trend was the complete opposite.

- For example, lower ABL total water mixing ratio and larger Bowen ratio delay cloud dissipation with co-variability while they accelerate dissipation time as single variables or in previous studies (Ghonima et al. 2016).

- Co-variability also provides a different perspective on how sea-breeze advection can affect dissipation time compared to previous Sc studies over coastal land (Ghonima et al. 2016), affecting initially thinner clouds more than thicker ones.

- Co-variability effects are uniquely observable in our analysis and could not have been observed with a traditional sensitivity analysis. The use of a model instead of observed data ensures that the trends observed are solely a consequence of the co-variability in the dataset and not of unknown or unobservable effects stemming from real-world complexities. Given the importance of co-variability, modeling studies with sensitivity analyses should include co-variability in the scenario generation.

- Dissipation times predicted by the MLM correlate only weakly to observed dissipation times, likely due to the simplicity of the model.

Future work should examine correlations in other coastal Sc regions in order to study the extent of regional influence on the variables. Another topic of interest is the influence of realistic wind conditions on coastal dissipation time.

Acknowledgments. We thank E. Wu, H. Yang, B. Akyurek, and X. Zhong for helpful discussion and comments for this work. We thank the reviewers for their comments that improved the manuscript. MZZ is funded by CONICYT PFCHA/DOCTORADO BECAS CHILE/2015 - 72160605. The authors declare no conflict of interest. We thank Minghua Ong for editorial assistance.

APPENDIX A

Nomenclature

Roman symbols

A	In-cloud entrainment efficiency
A_{CBL}	Convective ABL entrainment efficiency
A_1, A_2	Constants for the shortwave radiative flux
c_1, c_2	Constants for the longwave radiative flux
C_f	Bulk transfer coefficient for surface fluxes
C_p	Mean heat capacity of dry air in the ABL

d^2	Squared distance for the STI method
D	ABL large-scale horizontal divergence
f_w	Filter for westerly wind
F	Total net radiative flux
F_{LW}	Net longwave radiation flux
F_{SW}	Net shortwave radiation flux
g	Gravitational acceleration
h	Cloud thickness
k	Constant for the shortwave radiative flux
L_{lv}	Mean latent heat of vaporization in the ABL
$\mathrm{LW}\downarrow_{\mathrm{i}}$	Downwelling longwave flux at z_i
n_b^{RH}	Points below z_b^{RH} in the radiosonde
p	Pressure
p_{00}	Reference pressure (1000 hPa)
q	Constant for the shortwave radiative flux
q_l	Liquid water mixing ratio
q_{sat}	Water saturation mixing ratio
q_t	Total water mixing ratio
q_v	Water vapor mixing ratio
R_d	Specific gas constant for dry air
R_v	Specific gas constant for water vapor
Ri	Bulk Richardson number
$\mathbf{s}$	Auxiliary variable for the STI method

SW_i	Shortwave irradiance above the cloud
t_{diss}	Predicted dissipation time
T_b	Temperature at cloud base
T_{cld}	Mean cloud temperature
T_{sc}	Mean temperature below cloud
T_{sky}	Effective sky temperature
u	Wind speed for large scale advection
$\mathbf{u}(t)$	Wind velocity vector
$\overline{u}$	16 h average wind speed
$\overline{w'\theta_l'}$	Vertical turbulent flux of θ_l
$\overline{w'\theta_v'}$	Buoyancy flux
$\overline{w'q_t'}$	Vertical turbulent flux of q_t
w_*	Convective vertical velocity scale
w_e	Entrainment rate
w_{sub}	Subsidence rate
z	Height
z_b	Cloud-base height
z_b^{RH}	Radiosonde cloud-base height
$z_i\|_h$	Changes of z_i maintaining constant h
z_i	Inversion base height
z_i^+	Just above inversion base height
z_{it}	Inversion top height

Greek symbols

α	Constant for the longwave radiative flux
$\alpha_w(t)$	Wind direction
β	Constant for the shortwave radiative flux
γ	Constant for the longwave radiative flux
$\delta\psi/\delta t_{diss}$	Change in ψ to delay t_{diss} by 1 h
Δx	Distance between ocean and land columns
ΔT	Temperature inversion strength
θ	Potential temperature
θ_l	Liquid water potential temperature
θ_v	Virtual potential temperature
μ_0	Cosine of the solar zenith angle
ξ	Tuning parameter for the STI method
Π	Exner function
ρ	Air density in the ABL
σ	Stefan-Boltzmann constant
$\tau_{\mathrm{SW}}(z)$	Cloud optical depth for shortwave radiation (zero at cloud top)
$\tau_{\mathrm{LW}}(z)$	Cloud optical depth for longwave radiation (zero at cloud top)
$\tau_{\mathrm{LW,b}}$	Cloud optical depth at cloud base for longwave radiation
ϕ	Conversion efficiency for land surface fluxes
ω	Pressure vertical velocity
∇_h	Horizontal gradient operator

Abbreviations

Bo	Bowen ratio
GHI	Global Horizontal Irradiance
LHF	Latent heat flux at the ocean surface
LTS	Lower Tropospheric Stability
MLM	Mixed-Layer Model
Sc	Stratocumulus
SHF	Sensible heat flux at the ocean surface
STI	Steady Thickness Initialization
SZA	Solar zenith angle

Subscripts and superscripts

ψ^{BL}	Well-mixed value of ψ in the ABL
$\psi^{3\mathrm{km}}$	Value of ψ at $z = 3$ km
ψ_0	Value of ψ at the surface
ψ_b	Value of ψ at the cloud base
ψ_{cld}	Value of ψ evaluated in the cloud region
ψ_i	Value of ψ at the inversion base
$(\psi)_{new}$	New value of ψ to maintain constant h
$(\psi)_{old}$	Original value of the variable ψ
$\Delta_i\psi$	Inversion jump of ψ

APPENDIX B

Mixed-Layer Model

B1. Governing equations

The state of the well-mixed ABL is described by inversion base height z_i, total water mixing ratio $q_t = q_v + q_l$, and liquid water potential temperature $\theta_l \approx \theta - \frac{L_{lv} q_l}{C_p \Pi}$, where q_v is the water vapor mixing ratio, q_l is the liquid water mixing ratio, $\Pi = (p/p_{00})^{R_d/C_p}$ is the Exner function, L_{lv} is the latent heat of vaporization, C_p is the heat capacity of dry air, p is pressure, $p_{00} = 1000$ hPa, and R_d is the specific gas constant for dry air.

The governing equations of the MLM are the air mass, energy, and moisture balances (Eqs. B1, B3, B4), which describe the average state of the ABL through the well-mixed variables q_t^{BL} and θ_l^{BL}. In the air mass balance (Eq. B1), entrainment, subsidence velocity, and large-scale advection determine the evolution of the ABL depth z_i.

$$\frac{\partial z_i}{\partial t} = w_e + w_{sub} - u \nabla_h z_i, \tag{B1}$$

where w_e is the entrainment rate, w_{sub} is the subsidence rate, u is horizontal wind speed, and ∇_h is the large-scale horizontal gradient operator. The subsidence rate at the top of the ABL, w_{sub}, is parameterized by constant horizontal divergence D within the ABL:

$$w_{sub} = -D \cdot z_i. \tag{B2}$$

In the heat balance (Eq. B3), turbulent fluxes, radiation, and large-scale advection drive the evolution of the temperature in the ABL:

$$\frac{\partial \theta_l^{\mathrm{BL}}}{\partial t} = -\frac{\partial}{\partial z} \left(\overline{w' \theta_l'}(z) + \frac{F(z)}{\rho C_p} \right) - u \nabla_h \theta_l^{\mathrm{BL}}, \tag{B3}$$

where $\overline{w'\theta_l'}(z)$ is the turbulent flux of liquid potential temperature and $F(z)$ is the vertical profile of radiative flux.

In the total water content balance (Eq. B4), we do not consider precipitation fluxes and subsequently, only turbulent fluxes and large-scale advection are present:

$$\frac{\partial q_t^{\mathrm{BL}}}{\partial t} = -\frac{\partial}{\partial z}\overline{w'q_t'}(z) - u\nabla_h q_t^{\mathrm{BL}}, \tag{B4}$$

where $\overline{w'q_t'}(z)$ is the turbulent flux of total water mixing ratio.

B2. Horizontal advection

To describe ocean-land interaction, we model the evolution of two columns: one over the ocean and the other over land (Fig. 1). Due to the dominant wind direction from the ocean to the land, the ocean column model does not contain any advection terms, i.e. the last terms in (Eqs. B1, B3, B4) are removed. For the land column, the advection terms depend on both ocean and land conditions.

$$u\nabla_h \theta_l^{\mathrm{BL}} = \frac{u}{\Delta x}(\theta_{l,\mathrm{land}}^{\mathrm{BL}} - \theta_{l,\mathrm{ocean}}^{\mathrm{BL}}) \tag{B5}$$

$$u\nabla_h q_t^{\mathrm{BL}} = \frac{u}{\Delta x}(q_{t,\mathrm{land}}^{\mathrm{BL}} - q_{t,\mathrm{ocean}}^{\mathrm{BL}}), \tag{B6}$$

where u is the wind speed and $\Delta x = 30$ km is the distance between the two columns. The associated coupling timescales $\Delta x/u$ range between 1.3 h and 3.6 h min at noon, when the wind speed is maximum, and between 3.1 h and 8.4 h at night.

B3. Entrainment parameterization

The entrainment rate is parameterized through buoyancy flux contributions (Ghonima et al. 2016, Section 4b). The total entrainment rate is the sum of contributions from surface and cloud regions, where each amount is proportional to a convective velocity scale, w_*, and inversely proportional to a bulk Richardson number, Ri.

$$w_e = w_{e,0} + w_{e,cld} = A_{\mathrm{CBL}}\frac{w_{*0}}{\mathrm{Ri}_0} + A\frac{w_{*cld}}{\mathrm{Ri}_{\mathrm{cld}}} = 1.25\frac{A_{\mathrm{CBL}}}{\Delta_i\theta_v}\overline{w'\theta_v'}|_0 + 2.5\frac{A}{h\Delta_i\theta_v}\int_{z_b}^{z_i}\overline{w'\theta_v'}(z)dz, \tag{B7}$$

where, at the surface, the constant $A_{\mathrm{CBL}} = 0.2$ (Deardorff 1976) is a clear convective boundary layer (CBL) entrainment efficiency, w_{*0} is the surface convective velocity scale, and Ri_0 is the surface bulk Richardson number. For the cloud region, A is an entrainment efficiency coefficient (Grenier and Bretherton 2001) that includes evaporative enhancement effects, w_{*cld} is a cloud convective velocity scale, and $\mathrm{Ri}_{\mathrm{cld}}$ is the bulk Richardson number in the cloud region. Lastly, $\Delta_i\theta_v$ is the inversion jump of virtual potential temperature, and $\overline{w'\theta_v'}(z)$ is the buoyancy flux with $\overline{w'\theta_v'}|_0$ as its surface value. The buoyancy flux uses a vertical profile of dry and moist coefficients that were updated at each iteration and were calculated differently for the subcloud and cloud regions, following Cuijpers and Duynkerke (1993, Appendix A).

Some cases resulted in negative entrainment when using this paramterization, and were discarded from the analysis. When analyzing the entrainment rate, algebraic manipulation yields an explicit equation:

$$w_e = \frac{w_{e,0} + \frac{2.5A}{h\Delta_i\theta_v}\int_{z_b}^{z_i}\left(C_1\left[\left(1-\frac{z}{z_i}\right)\left(\overline{w'\theta_l'}|_0 + \frac{F_0}{\rho C_p}\right) + \frac{z}{z_i}\frac{F_i}{\rho C_p} - \frac{F(z)}{\rho C_p}\right] + C_2\left[\left(1-\frac{z}{z_i}\right)\overline{w'q_t'}|_0\right]\right)dz}{1 + \frac{2.5A}{h\Delta_i\theta_v}\int_{z_b}^{z_i}\frac{z}{z_i}(C_1\Delta_i\theta_l + C_2\Delta_i q_t)dz}, \tag{B8}$$

where C_1 and C_2 are the moist coefficients. The denominator can be negative depending on the value of the integral. Assuming C_1 and C_2 are constants (which is a reasonable assumption), the criterion for negative entrainment becomes

$$\frac{h}{2z_i}(C_1\Delta_i\theta_l + C_2\Delta_i q_t) < -\frac{\Delta_i\theta_v}{2.5A}, \tag{B9}$$

which depends on many parameters and cannot be analyzed in a simple way. If we explore the condition for r.h.s.$= 0$, with referential moist coefficients $C_1 = 0.5$ and $C_2 = 970$ K (Ghonima et al. 2016, Section 4b), we obtain: $\Delta_i\theta_l < C_2/C_1|\Delta_i q_t| \approx 1.94|\Delta_i q_t|$. The CTEI criterion also relates the inversion jumps (van der Dussen et al. 2013, Eq. (1)) and can be rewritten as $\Delta_i\theta_l < 0.77\, L_{lv}/C_p|\Delta_i q_t| \approx 1.915|\Delta_i q_t|$. Both conditions are very similar, suggesting that the cases close to the critical CTEI criterion can yield negative entrainment rates when using this parameterization. Our physical interpretation is that for cases where negative subcloud fluxes should develop, the integrated buoyancy flux in the ABL cannot be described by the positive in-cloud buoyancy flux alone, resulting in an artificial negative entrainment velocity.

B4. Radiative model

The net upward radiative flux includes longwave and shortwave contributions: $F = F_{\mathrm{LW}} - F_{\mathrm{SW}}$.

$$\begin{aligned} F_{\mathrm{SW}}(z) = \frac{4}{3}\mathrm{SW_i}(qA_1 e^{-k\tau_{\mathrm{SW}}(z)} - qA_2 e^{k\tau_{\mathrm{SW}}(z)} \\ -\beta e^{-\tau_{\mathrm{SW}}(z)/\mu_0}) + \mu_0 \mathrm{SW_i} e^{-\tau_{\mathrm{SW}}(z)/\mu_0}, \end{aligned} \tag{B10}$$

where SZA is the solar zenith angle, $\mu_0 = \cos(\mathrm{SZA})$, $\tau_{\mathrm{SW}}(z)$ is the cloud optical depth (zero at cloud top) (Duynkerke et al. 2004, Eqs. 6 and 7) calculated with an effective radius of 10 μm, A_1 and A_2 come from boundary conditions of the radiative transfer equation, and k, q and β are constants that depend on μ_0 and optical properties of cloud droplets (Duynkerke et al. 2004, Appendix).

The longwave contribution F_{LW} depends on three temperatures: T_{sc} taken as the mean temperature of the subcloud region; T_{cld} taken as the mean temperature in the cloud region, and T_{sky} taken as an effective radiative temperature of the sky.

$$\begin{aligned} F_{\mathrm{LW}}(z) = \gamma\sigma[(T_{cld}^4 - T_{sky}^4)c_1 e^{-\alpha\tau_{\mathrm{LW},b}} + (T_{sc}^4 - T_{cld}^4)c_2]e^{\alpha\tau_{\mathrm{LW}}(z)} \\ +[(T_{cld}^4 - T_{sky}^4)c_2 e^{\alpha\tau_{\mathrm{LW},b}} + (T_{sc}^4 - T_{cld}^4)c_1]e^{-\alpha\tau_{\mathrm{LW}}(z)}, \end{aligned} \tag{B11}$$

where σ is the Stefan-Boltzmann constant, $\tau_{\mathrm{LW}}(z)$ is the cloud optical depth (Larson et al. 2007, Eqs. 6 and 7), and $\tau_{\mathrm{LW},b}$ is the maximum optical depth (at cloud base). The parameters α, c_1, c_2, and γ are terms derived from the radiation transfer equation (Ghonima et al. 2016, Appendix B).

B5. Surface and cloud-top fluxes

The surface fluxes of moisture $\overline{w'q_t'}|_0$ and temperature $\overline{w'\theta_l'}|_0$ depend on the type of the surface. For the ocean column, the SHF and LHF are fixed during the day. For the land column, the surface fluxes depend on the Bowen ratio Bo. A part of the net radiation flux at the surface F_0 is converted into a moisture and a heat flux released to the ABL (Eqs. B12, B13).

$$\overline{w'q_t'}|_{0,\mathrm{land}} = \phi \frac{1}{1+\mathrm{Bo}} \frac{F_0}{\rho C_p} \tag{B12}$$

$$\overline{w'\theta_l'}|_{0,\mathrm{land}} = \phi \frac{\mathrm{Bo}}{1+\mathrm{Bo}} \frac{F_0}{\rho C_p}, \tag{B13}$$

where $\phi = 0.88$ is the efficiency at which net radiation is converted into surface fluxes (Ghonima et al. 2016).

At the top of the ABL, the turbulent fluxes of moisture $\overline{w'q_t'}|_i$ and temperature $\overline{w'\theta_l'}|_i$ depend on the entrainment rate w_e and the sharp inversion jumps of moisture (Eq. B14) and temperature (Eq. B15), respectively (Lilly 1968):

$$\overline{w'q_t'}|_i = -w_e \Delta_i q_t, \tag{B14}$$

$$\overline{w'\theta_l'}|_i = -w_e \Delta_i \theta_l. \tag{B15}$$

APPENDIX C

Data

C1. Variables

The parameterizations and equations included in the MLM determine our variables of interest. We gather data from different sources for the years 2014 to 2017, May to September. In the following, variables are grouped by their data source.

C2. Radiosondes: z_i, $\theta_l(z)$, $q_t(z)$

We obtain 1200 UTC radiosonde data (reported at 0400 LST, launched at 0300 LST) from the NKX Miramar Marine Corps Air Station in Southern California (32.85° N, 117.2°W). The station is located 10 km away from the coast, where the shoreline is aligned meridionally.

Radiosonde profiles are post-processed into well-mixed layers to make them compatible with the MLM. First, temperature inversions in the lowest 3 km are detected. The largest temperature inversion is assumed to cap the mixed layer if it is sufficiently strong ($\Delta T > 3$ K), yielding inversion base and top heights, z_i and z_{it} respectively. Clouds are assumed to exist where relative humidity (RH) exceeds 95% below z_i, with the radiosonde cloud base z_b^{RH} defined as the lowest point that meets that condition. Decoupled days cannot be represented in an MLM, and thus, we discard these days using the criterion $|\theta_{vb} - \theta_{v0}| > 1\ K$ (Ghate et al. 2015), where θ_{vb} and θ_{v0} are the virtual potential temperature at the radiosonde cloud base and at the surface, respectively.

The well-mixed q_t (Eq. C1) is an ABL average of the radiosonde measurements. Since q_l is not measured by radiosondes, q_t will be underestimated, but in view of the limited resolution of the data and that $q_t \gg q_l$, this approach is reasonable. Above the inversion, we consider q_t to be constant, and also compute it as an average up to 3 km.

$$q_t(z) = \begin{cases} q_t^{\mathrm{BL}} = \dfrac{1}{z_i}\displaystyle\int_0^{z_i} q_v(z)dz & \text{if } z < z_i \\ q_t^{\mathrm{3km}} = \dfrac{1}{3\text{ km} - z_{it}}\displaystyle\int_{z_{it}}^{3\text{ km}} q_v(z)dz & \text{if } z \geq z_i. \end{cases} \tag{C1}$$

For $\theta_l(z)$, we follow a similar averaging approach (Eq. C2). If there are more than 5 data points below z_b^{RH}, the average is computed in the subcloud region to avoid phase-change heating effects on $\theta(z)$; otherwise, all points in the ABL are averaged (including all the points is not a major concern for q_t since $q_t \gg q_l$). Above the ABL, we obtain a linear fit for $\theta(z_{it} < z < 3$ km$)$.

$$\theta_l(z) = \begin{cases} \theta_l^{\mathrm{BL}} = \dfrac{1}{z_i}\displaystyle\int_0^{z_i} \theta(z)dz & \text{if } z < z_i \text{ and } n_b^{\mathrm{RH}} \leq 5 \\ \theta_l^{\mathrm{BL}} = \dfrac{1}{z_b^{\mathrm{RH}}}\displaystyle\int_0^{z_b^{\mathrm{RH}}} \theta(z)dz & \text{if } z < z_i \text{ and } n_b^{\mathrm{RH}} > 5 \\ a \cdot z + b & \text{if } z \geq z_i \text{ with } a, b \text{ from linear fit for } \theta(z_{it} < z < 3\text{ km}), \end{cases} \tag{C2}$$

where n_b^{RH} is the number of points below z_b^{RH}.

We assume that the inversion occurs over an infinitesimally thin layer, defining the inversion jumps of total water mixing ratio and liquid water potential temperature:

$$\Delta_i q_t = q_t^{3\mathrm{km}} - q_t^{\mathrm{BL}}, \tag{C3}$$

$$\Delta_i \theta_l = \theta_l(z = z_i^+) - \theta_l^{\mathrm{BL}}, \tag{C4}$$

where z_i^+ is just above the inversion height.

C3. Radiative and clear sky models: T_{sky} and SW_i

We obtain the effective sky temperature T_{sky} for the longwave radiative model using the Streamer radiative transfer model (Key and Schweiger 1998). Inputs are the temperature and relative humidity soundings, which are extended to 100 km with a *U.S. Standard Atmosphere, 1976*. We compute T_{sky} as the blackbody temperature from the longwave downwelling flux at the top of the cloud as $\mathrm{LW}\downarrow_i = \sigma T_{sky}^4$. Fig. B1-a shows that skies with more water content experience a smaller net radiative cooling at the cloud top.

For the shortwave radiation model, SW_i is the solar irradiance incident on the top of the Sc cloud. We estimate SW_i as the global horizontal irradiance (GHI) from a clear sky model (Ineichen and

Perez 2002). Monthly climatological Linke turbidities for that location are input to the clear sky model.

C4. NWP models: Bo, D

We estimate the Bowen ratio Bo at NKX by analyzing in-house operational runs of the Weather Research and Forecasting (WRF) model using the Noah land surface model (Skamarock et al. 2008). Bo is the ratio between SHF and LHF at the surface at the nearest grid point to the NKX station. Hourly output is averaged between 0800 and 1500 LST to yield a (constant) daily Bo that is input to the MLM simulations. Land surface models in WRF are known to differ from measurements (Wharton et al. 2016); land surface models tend to produce Bo ≈ 1 with small temporal deviations.

We estimate large-scale divergence D from the NAM Forecasting System as the partial derivative of pressure vertical velocity ω with respect to pressure in the ABL. The differences are computed between 975 hPa and 850 hPa (Eq. C5). We average D spatially over an area of 21 grid points over the ocean around (38.15°N, 117.5°W) and then temporally with a 3-day moving average:

$$D = -\frac{\partial \omega}{\partial p} \approx -\frac{\omega(975\ \mathrm{hPa}) - \omega(850\ \mathrm{hPa})}{975\ \mathrm{hPa} - 850\ \mathrm{hPa}}. \tag{C5}$$

C5. METAR and NDBC: $\overline{u}$, SLP, SHF, LHF

For coastal regions in Southern California, the sea breeze acts during the day with a strong westerly component, usually beginning around 0800 LST and peaking around 1200 LST. A 16 h average (between 0500 and 2100 LST) wind speed $\overline{u}$ is computed from the METAR weather station at NKX. All westerly winds (with direction between 180° and 360°) are scalar-averaged (Eq. C6).

$$\overline{u} = \frac{1}{16\ \mathrm{h}} \int_{t=0500\ \mathrm{LST}}^{t=2100\ \mathrm{LST}} f_w(\mathbf{u}(t))dt, \tag{C6}$$

where $\mathbf{u}(t)$ is the wind velocity with magnitude $u(t)$ and direction $\alpha_w(t)$ and $f_w(\mathbf{u}(t))$ is the filter for considering westerly directions only:

$$f_w(\mathbf{u}) = \begin{cases} u(t) & \text{if } \alpha_w(t) \in (180°, 360°) \\ 0 & \text{else.} \end{cases} \tag{C7}$$

A 10-year average daily wind profile is shown in Fig. B1-b. The daily profile is normalized by its 16 h average wind speed and then re-scaled with the daily $\overline{u}$.

We estimate SLP as the daily average SLP at the METAR weather station at NKX.

Surface turbulent fluxes in the ocean column, which are fixed in the MLM, are computed from wind and sea surface temperature data. Daily averages of SST are obtained at the Torrey Pines Outer station from the National Data Buoy Center (NDBC) (NOAA 2017). Surface fluxes are computed using a bulk transfer coefficient $C_f = 1.2 \times 10^{-3}$ (Blossey et al. 2013), the average SST and wind speed, and assuming that the temperature and moisture above the surface is the same as that of the initial state of the ABL (Eqs. C8, C9):

$$\mathrm{SHF} = \rho C_p \overline{u} C_f (\mathrm{SST} - \theta_l^{\mathrm{BL}}), \tag{C8}$$

$$\mathrm{LHF} = \rho L_{lv} \overline{u} C_f (q_{sat}(\mathrm{SST}) - q_t^{\mathrm{BL}}), \tag{C9}$$

where q_{sat} is the saturation mixing ratio.

APPENDIX D

Dissipation time comparison

We estimate dissipation time over NKX t_{diss}^{SAT} using a satellite derived low cloudiness product (Clemesha et al. 2016; Wu et al. 2018). This dataset has a 4 km spatial resolution and 30-minute time resolution. We obtain t_{diss}^{SAT} at the closest pixel to NKX as the time when skies are clear for at least 1 hour afterwards. We neglect t_{diss}^{SAT} before 0500 LST since they are unlikely to caused by Sc, which would thicken during the night.

We also estimate dissipation time t_{diss}^{GHI} from 1 s global horizontal irradiance data measurements at the UC San Diego campus, 5 km west of NKX (Zamora Zapata et al. 2019). Only Sc to clear transitions are included; a Sc cloud is assumed to exist if the early sounding is well-mixed and has a cloud presence (RH>95%), while also checking sky imagery at the time of the breakup to discard other cloud types or the presence of upper lever clouds. A t_{diss}^{GHI} event is recorded when the clear sky index is close to 1 for the following 5 minutes.

There is a strong correlation between t_{diss}^{SAT} and t_{diss}^{GHI} (0.79, $\mathrm{R}^2 = 0.6$), while the correlation between MLM modeled dissipation time and t_{diss}^{SAT} and t_{diss}^{GHI} is 0.26 and 0.28 with R^2 of 0.06 and 0.07, respectively.

Ideally the MLM dissipation times would be more correlated to the observed dissipation times. But given the MLM assumptions, parameter uncertainties, adjustment of initial conditions, and neglect of some physical processes, the relatively small correlation is not surprising. We maintain that the MLM based analysis of parameter correlations is valuable and superior to the alternatives. Strengths of the MLM application in this analysis include: (i) The MLM represents most of the physical processes. (ii) The MLM has been validated by Ghonima et al. (2016) against LES, demonstrating that the MLM is capable of correctly predicting the evolution of an idealized coastal Sc cloud. (iii) Initial conditions are approximated through elaborate sourcing from best available models and measurement sources. (iv) The simple geometric domain of the MLM prevents real-world complexities such as varying topography and 3D effects from affecting the results. (v) Simulation days are limited to conditions that are represented in the model, e.g. days with decoupling are removed. However, as evidenced by the need for adjustment of initial conditions, there are inconsistencies in the initial conditions and/or shortcomings in the model. As a result the MLM results live in a virtual / model world. But we maintain that to analyze variability and co-variability between variables an internally consistent albeit somewhat idealistic modeling approach is preferable over sparse measurements and 3D models such as WRF that also perform poorly and introduce additional complexities. This paper is the first to attempt a comprehensive evaluation of variability and co-variability of atmospheric parameters for Sc dissipation over land. It is our hope that in the future models are improved and models can be better coupled to measurements to narrow the gap between model results and observations.

APPENDIX E

Linear approximation to $q_t^{\mathrm{BL}}(z_i, \theta_l^{\mathrm{BL}})$

For a cloud to form given ABL height z_i and well-mixed liquid water potential temperature θ_l^{BL}, the total water content at ABL top must surpass saturation by a small amount, which is condensed into a cloud: $q_t^{\mathrm{BL}} = q_{sat}(z_i, \theta_l^{\mathrm{BL}}) + q_l(z_i)$. Since $q_l(z_i) << q_t^{\mathrm{BL}}$, we investigate the behavior of $q_{sat}(z, \theta_l)$:

$$q_{sat} = \frac{\varepsilon}{p(z)/e_s(z, \theta_l) - 1}, \tag{E1}$$

where $\varepsilon = 0.622$ and pressure follows the hydrostatic assumption $p(z) \approx p_0 - \rho g z$. The water saturation pressure e_s is given by the August-Roche-Magnus approximation:

$$e_s = \kappa_1 \exp\left(\frac{\kappa_2 T_c}{\kappa_3 + T_c}\right), \tag{E2}$$

where $\kappa_1 = 610.94$ Pa, $\kappa_2 = 17.625$, $\kappa_3 = 243.04$, and T_c is temperature in Celsius. To estimate temperature near the cloud top, we will assume that we are just surpassing saturation with an infinitesimally thin cloud and use the dry adiabatic lapse rate.

$$T_c = T_0 - \Gamma_d z - 273.15 \text{ K}, \tag{E3}$$

where $\Gamma_d = g/C_p$ is the dry adiabatic lapse rate and T_0 is surface temperature, which is related to the well-mixed θ_l and surface pressure p_0:

$$T_0 = \theta_l \left(\frac{p_0}{p_{00}}\right)^{R_d/C_p}. \tag{E4}$$

With these assumptions, we can estimate $\frac{\partial q_{sat}}{\partial z}$ and $\frac{\partial q_{sat}}{\partial \theta_l}$ and evaluate them at the observed means of z_i, θ_l, and p_0 (Table 1), obtaining

$$\frac{\partial q_{sat}}{\partial \theta_l} = \frac{\varepsilon p}{(\frac{p}{e_s}-1)^2} \frac{p\kappa_2\kappa_3}{e_s(\kappa_3+T_c)^2} \approx 0.6964 \text{ g kg}^{-1}\text{K}^{-1}, \tag{E5}$$

$$\frac{\partial q_{sat}}{\partial z} = \frac{-\varepsilon}{(\frac{p}{e_s}-1)^2} \frac{\frac{p\kappa_2\Gamma_d\kappa_3 e_s}{(\kappa_3+T_c)^2} - \rho g e_s}{e_s^2} \approx -0.0055\text{g kg}^{-1}\text{m}^{-1}, \tag{E6}$$

which yields results similar to the linear fit coefficients in Fig. 7-a. This indicates that even with the assumptions made here, the linear relationship between z_i, θ_l^{BL}, and q_t^{BL} closely follows the saturation condition.

APPENDIX F

Fig. F1 here

References

Akyurek, B. O., and J. Kleissl, 2017: Closed-Form Analytic Solution of Cloud Dissipation for a Mixed-Layer Model. *J. Atmos. Sci.*, **74 (8)**, 2525–2556, doi:10.1175/JAS-D-16-0303.1.

Blossey, P. N., and Coauthors, 2013: Marine low cloud sensitivity to an idealized climate change: The CGILS LES intercomparison. *J. Adv. Model. Earth Syst.*, **5 (2)**, 234–258, doi:10.1002/jame.20025.

Bony, S., and J.-L. Dufresne, 2005: Marine boundary layer clouds at the heart of tropical cloud feedback uncertainties in climate models. *Geophys. Res. Lett.*, **32 (20)**, L20 806, doi:10.1029/2005GL023851.

Bretherton, C. S., and M. C. Wyant, 1997: Moisture Transport, Lower-Tropospheric Stability, and Decoupling of Cloud-Topped Boundary Layers. *J. Atmos. Sci.*, **54 (1)**, 148–167, doi:10.1175/1520-0469(1997)054⟨0148:MTLTSA⟩2.0.CO;2.

Burleyson, C. D., and S. E. Yuter, 2015: Patterns of Diurnal Marine Stratocumulus Cloud Fraction Variability. *J. Appl. Meteor. Climatol.*, **54**, 847–866, doi:10.1175/JAMC-D-14-0178.1.

Chlond, A., and A. Wolkau, 2000: Large-Eddy Simulation Of A Nocturnal Stratocumulus-Topped Marine Atmospheric Boundary Layer: An Uncertainty Analysis. *Bound.-Layer Meteor.*, **95**, 31–55, doi:10.1023/A:1002438701638.

Christensen, M. W., G. G. Carrió, G. L. Stephens, and W. R. Cotton, 2013: Radiative Impacts of Free-Tropospheric Clouds on the Properties of Marine Stratocumulus. *J. Atmos. Sci.*, **70 (10)**, 3102–3118, doi:10.1175/JAS-D-12-0287.1.

Clemesha, R. E. S., A. Gershunov, S. F. Iacobellis, A. P. Williams, and D. R. Cayan, 2016: The northward march of summer low cloudiness along the California coast. *Geophys. Res. Lett.*, **43 (3)**, 1287–1295, doi:10.1002/2015GL067081.

Cuijpers, J. W. M., and P. G. Duynkerke, 1993: Large eddy simulation of trade wind cumulus clouds. *J. Atmos. Sci.*, **50 (23)**, 3894–3908, doi:10.1175/1520-0469(1993)050⟨3894:LESOTW⟩2.0.CO;2.

Dal Gesso, S., A. P. Siebesma, S. R. de Roode, and J. M. van Wessem, 2014: A mixed-layer model perspective on stratocumulus steady states in a perturbed climate. *Quart. J. Roy. Meteor. Soc.*, **140 (684)**, 2119–2131, doi:10.1002/qj.2282.

Deardorff, J. W., 1976: On the entrainment rate of a stratocumulus-topped mixed layer. *Quart. J. Roy. Meteor. Soc.*, **102 (433)**, 563–582, doi:10.1002/qj.49710243306.

Deardorff, J. W., 1980: Cloud Top Entrainment Instability. *Journal of the Atmospheric Sciences*, **37 (1)**, 131–147, doi:10.1175/1520-0469(1980)037⟨0131:CTEI⟩2.0.CO;2, URL https://journals.ametsoc.org/doi/abs/10.1175/1520-0469%281980%29037%3C0131%3ACTEI%3E2.0.CO%3B2.

Duynkerke, P. G., and J. Teixeira, 2001: Comparison of the ECMWF Reanalysis with FIRE I Observations: Diurnal Variation of Marine Stratocumulus. *J. Climate*, **14 (7)**, 1466–1478, doi:10.1175/1520-0442(2001)014⟨1466:COTERW⟩2.0.CO;2.

Duynkerke, P. G., and Coauthors, 2004: Observations and numerical simulations of the diurnal cycle of the EUROCS stratocumulus case. *Quart. J. Roy. Meteor. Soc.*, **130 (604)**, 3269–3296, doi:10.1256/qj.03.139.

Fang, M., B. A. Albrecht, V. P. Ghate, and P. Kollias, 2014: Turbulence in Continental Stratocumulus, Part I: External Forcings and Turbulence Structures. *Bound.-Layer Meteor.*, **150 (3)**, 341–360, doi:10.1007/s10546-013-9873-3.

Ghate, V. P., M. A. Miller, B. A. Albrecht, and C. W. Fairall, 2015: Thermodynamic and Radiative Structure of Stratocumulus-Topped Boundary Layers. *J. Atmos. Sci.*, **72**, 430–451, doi:10.1175/JAS-D-13-0313.1.

Ghonima, M. S., J. R. Norris, T. Heus, and J. Kleissl, 2015: Reconciling and Validating the Cloud Thickness and Liquid Water Path Tendencies Proposed by R. Wood and J. J. van der Dussen et al. *J. Atmos. Sci.*, **72 (5)**, 2033–2040, doi:10.1175/JAS-D-14-0287.1.

Ghonima, M. S., J. R. Norris, and J. Kleissl, 2016: Factors controlling stratocumulus cloud lifetime over coastal land. *J. Atmos. Sci.*, **73**, 2961–2983, doi:10.1175/JAS-D-15-0228.1.

Grenier, H., and C. S. Bretherton, 2001: A Moist PBL Parameterization for Large-Scale Models and Its Application to Subtropical Cloud-Topped Marine Boundary Layers. *Mon. Wea. Rev.*, **129 (3)**, 357–377, doi:10.1175/1520-0493(2001)129⟨0357:AMPPFL⟩2.0.CO;2.

Halliwell, G. R., and J. S. Allen, 1987: The large-scale coastal wind field along the west coast of North America, 1981-1982. *J. Geophys. Res. Oceans*, **92**, 1861–1884, doi:10.1029/JC092iC02p01861.

Hanson, H. P., 1990: Marine stratocumulus climatologies. *Int. J. Climatol.*, **11 (2)**, 147–164, doi:10.1002/joc.3370110204.

Hartmann, D. L., M. E. Ockert-Bell, and M. L. Michelsen, 1992: The Effect of Cloud Type on Earth's Energy Balance: Global Analysis. *J. Climate*, **5 (11)**, 1281–1304, doi:10.1175/1520-0442(1992)005⟨1281:TEOCTO⟩2.0.CO;2.

Ineichen, P., and R. Perez, 2002: A new airmass independent formulation for the Linke turbidity coefficient. *Solar Energy*, **73 (3)**, 151–157, doi:10.1016/S0038-092X(02)00045-2.

Jamaly, M., J. L. Bosch, and J. Kleissl, 2013: Aggregate Ramp Rates of Distributed Photovoltaic Systems in San Diego County. *IEEE Trans. Sustainable Energy*, **4 (2)**, 519–526, doi:10.1109/TSTE.2012.2201966.

Key, J. R., and A. J. Schweiger, 1998: Tools for atmospheric radiative transfer: Streamer and FluxNet. *Comput. Geosci.*, **24 (5)**, 443 – 451, doi:10.1016/S0098-3004(97)00130-1.

Klein, S. A., and D. L. Hartmann, 1993: The seasonal cycle of low stratocumulus clouds. *J. Climate*, **6 (8)**, 1587–1606, doi:10.1175/1520-0442(1993)006⟨1587:TSCOLS⟩2.0.CO;2.

Klein, S. A., D. L. Hartmann, and J. R. Norris, 1995: On the Relationships among Low-Cloud Structure, Sea Surface Temperature, and Atmospheric Circulation in the Summertime Northeast Pacific. *J. Climate*, **8 (5)**, 1140–1155, doi:10.1175/1520-0442(1995)008⟨1140:OTRALC⟩2.0.CO;2.

Kopec, M. K., S. P. Malinowski, and Z. P. Piotrowski, 2016: Effects of wind shear and radiative cooling on the stratocumulus-topped boundary layer. *Quart. J. Roy. Meteor. Soc.*, **142 (701)**, 3222–3233, doi:10.1002/qj.2903.

Kuo, H.-C., and W. H. Schubert, 1988: Stability of cloud-topped boundary layers. *Quarterly Journal of the Royal Meteorological Society*, **114 (482)**, 887–916, doi:10.1002/qj.49711448204, URL https://rmets.onlinelibrary.wiley.com/doi/abs/10.1002/qj.49711448204.

Larson, V. E., K. E. Kotenberg, and N. B. Wood, 2007: An Analytic Longwave Radiation Formula for Liquid Layer Clouds. *Monthly Weather Review*, **135 (2)**, 689–699, doi:10.1175/MWR3315.1, URL https://journals.ametsoc.org/doi/abs/10.1175/MWR3315.1.

Lilly, D. K., 1968: Models of cloud-topped mixed layers under a strong inversion. *Quart. J. Roy. Meteor. Soc.*, **94 (401)**, 292–309, doi:10.1002/qj.49709440106.

Ma, Y.-F., J. G. Pedersen, W. W. Grabowski, M. K. Kopec, and S. P. Malinowski, 2018: Influences of Subsidence and Free-Tropospheric Conditions on the Nocturnal Growth of Nonclassical Marine Stratocumulus. *Journal of Advances in Modeling Earth Systems*, **10 (11)**, 2706–2730, doi: 10.1029/2018MS001295.

McMichael, L. A., D. B. Mechem, S. Wang, Q. Wang, Y. L. Kogan, and J. Teixeira, 2019: Assessing the mechanisms governing the daytime evolution of marine stratocumulus using large-eddy simulation. *Quart. J. Roy. Meteor. Soc.*, **145**, 845–866, doi:10.1002/qj.3469.

Mellado, J. P., 2017: Cloud-top entrainment in stratocumulus clouds. *Annu. Rev. Fluid Mech.*, **49 (1)**, 145–169, doi:10.1146/annurev-fluid-010816-060231.

Myers, T. A., and J. R. Norris, 2013: Observational Evidence That Enhanced Subsidence Reduces Subtropical Marine Boundary Layer Cloudiness. *J. Climate*, **26 (19)**, 7507–7524, doi:10.1175/JCLI-D-12-00736.1.

Nieuwstadt, F. T. M., and P. G. Duynkerke, 1996: Turbulence in the atmospheric boundary layer. *Atmospheric Research*, **40 (2)**, 111–142, doi:10.1016/0169-8095(95)00034-8, URL http://www.sciencedirect.com/science/article/pii/0169809595000348.

NOAA, 2017: National data buoy center - recent observations from buoy 46225 (32.933n 117.391w) - torrey pines outer, ca (100). URL http://www.ndbc.noaa.gov/station_page.php?station=46225.

Noda, A. T., K. Nakamura, T. Iwasaki, and M. Satoh, 2014: Responses of Subtropical Marine Stratocumulus Cloud to Perturbed Lower Atmospheres. *SOLA*, **10**, 34–38, doi:10.2151/sola.2014-008.

Seethala, C., J. R. Norris, and T. A. Myers, 2015: How Has Subtropical Stratocumulus and Associated Meteorology Changed since the 1980s? *J. Climate*, **28 (21)**, 8396–8410, doi:10.1175/JCLI-D-15-0120.1.

Skamarock, C., and Coauthors, 2008: A Description of the Advanced Research WRF Version 3. Tech. rep. doi:10.5065/D68S4MVH.

Stevens, B., 2004: Atmospheric moist convection. *Annual Review of Earth and Planetary Sciences*, **33 (1)**, 605–643, doi:10.1146/annurev.earth.33.092203.122658, URL https://www.annualreviews.org/doi/10.1146/annurev.earth.33.092203.122658.

van der Dussen, J. J., S. R. de Roode, S. Dal Gesso, and A. P. Siebesma, 2015: An LES model study of the influence of the free tropospheric thermodynamic conditions on the stratocumulus response to a climate perturbation. *J. Adv. Model. Earth Syst.*, **7**, 670–691, doi:10.1002/2014MS000380.

van der Dussen, J. J., S. R. de Roode, and A. P. Siebesma, 2013: Factors Controlling Rapid Stratocumulus Cloud Thinning. *J. Atmos. Sci.*, **71 (2)**, 655–664, doi:10.1175/JAS-D-13-0114.1.

van der Dussen, J. J., S. R. de Roode, and A. P. Siebesma, 2016: How large-scale subsidence affects stratocumulus transitions. *Atmos. Chemistry and Physics*, **16 (2)**, 691–701, doi:10.5194/acp-16-691-2016.

Wellby, S. J., and N. A. Engerer, 2015: Categorizing the Meteorological Origins of Critical Ramp Events in Collective Photovoltaic Array Output. *J. Appl. Meteor. Climatol.*, **55 (6)**, 1323–1344, doi:10.1175/JAMC-D-15-0107.1.

Wharton, S., M. Simpson, J. Osuna, J. Newman, and S. Biraud, 2016: The role of surface energy exchange for simulating wind inflow: An evaluation of multiple land surface models in WRF for the Southern Great Plains site field campaign report. Tech. Rep. DOE/SC-ARM-14-040. doi:10.2172/1254173.

Wood, R., 2012: Stratocumulus Clouds. *Mon. Wea. Rev.*, **140 (8)**, 2373–2423, doi:10.1175/MWR-D-11-00121.1.

Wood, R., and C. S. Bretherton, 2006: On the Relationship between Stratiform Low Cloud Cover and Lower-Tropospheric Stability. *J. Climate*, **19 (24)**, 6425–6432, doi:10.1175/JCLI3988.1.

Wu, E., R. E. S. Clemesha, and J. Kleissl, 2018: Coastal Stratocumulus cloud edge forecasts. *Solar Energy*, **164**, 355 – 369, doi:https://doi.org/10.1016/j.solener.2018.02.072.

Xu, X., and H. Xue, 2015: Impacts of Free-Tropospheric Temperature and Humidity on Nocturnal Nonprecipitating Marine Stratocumulus. *J. Atmos. Sci.*, **72 (8)**, 2853–2864, doi:10.1175/JAS-D-14-0387.1.

Zamora Zapata, M., E. Wu, and J. Kleissl, 2019: Irradiance enhancement events in the coastal stratocumulus dissipation process. *SWC 2019: ISES Solar World Congress*, Santiago, Chile.

Zelinka, M. D., D. A. Randall, M. J. Webb, and S. A. Klein, 2017: Clearing clouds of uncertainty. *Nature Climate Change*, **7**, 674–678, doi:10.1038/nclimate3402.

Zhu, P., and Coauthors, 2005: Intercomparison and Interpretation of Single-Column Model Simulations of a Nocturnal Stratocumulus-Topped Marine Boundary Layer. *Mon. Wea. Rev.*, **133**, 18, doi:10.1175/MWR2997.1.

LIST OF TABLES

TABLE 1. Statistics for the variables considered in the MLM initialization and complementary variables for describing the cloudy states, corresponding to the 195 available days. Original and STI derived states are included.

Original values

Variable	Units	Min	Max	Median	Mean	SD
q_t^{BL}	g kg^{-1}	7.557	16.38	11.51	11.52	1.494
$\Delta_i q_t$	g kg^{-1}	-10.89	-2.513	-7.246	-7.091	1.758
q_t^{3km}	g kg^{-1}	0.5531	12.59	4.217	4.424	2.278
θ_l^{BL}	K	287.9	298	291.8	291.7	1.697
$\Delta_i \theta_l$	K	5.679	19.53	11.04	11.3	2.538

STI modified values

Variable	Units	Min	Max	Median	Mean	SD
q_t^{BL}	g kg^{-1}	7.557	16.38	11.38	11.43	1.532
$\Delta_i q_t$	g kg^{-1}	-10.82	-2.513	-7.243	-7.073	1.749
q_t^{3km}	g kg^{-1}	0.2555	12.59	4.077	4.358	2.321
θ_l^{BL}	K	288.1	298	291.8	291.7	1.692
$\Delta_i \theta_l$	K	5.679	19.53	11.04	11.32	2.531

Unchanged values

Variable	Units	Min	Max	Median	Mean	SD
z_i	m	181	1493	587	597.8	190.8
z_{it}	m	322	1602	805	843.6	191.7
θ_l^{3km}	K	304.8	324.4	317	316.8	3.391
$\overline{u}$	m s^{-1}	1.543	4.148	2.458	2.531	0.4971
SLP	hPa	1008	1017	1012	1013	1.716
D	10^{-6} s^{-1}	-3.167	14.11	3.442	3.696	2.865
Bo	-	0.2293	1.563	1.053	1.047	0.1778
SW$_i$	W m^{-2}	827.4	989.5	977.5	961.5	33.75
LHF	W m^{-2}	8.385	75.18	31.82	32.54	11.44
SHF	W m^{-2}	1.222	19.24	8.661	8.829	3.312
SST	K	290.6	298.7	295	294.7	1.891
T_{sky}	K	255.7	291	272.4	272.2	6.608

Derived values

Variable	Units	Min	Max	Median	Mean	SD
z_b	m	159	1139	448	458.9	142.3
h	m	4	423	125	138.9	81.53
$\Delta_i \theta_v$	K	4.607	18.48	9.281	9.525	2.41
LWP	g m^{-2}	0.402	202.8	20.36	32.12	34.96

TABLE 2. Comparison of dissipation time trends for different variables; single variable changes from a reference case, and when all variables co-vary. Only the most robust trends are included.

1D Trend	Units	Single variations	Co-variability trends (95% CI)
$\delta z_i/\delta t_{diss}$	m h^{-1}	50.40	163.9 (130.6,219.8)
$\delta q_t^{\mathrm{BL}}/\delta t_{diss}$	g kg^{-1} h^{-1}	0.359	-2.826 (-5.465,-1.905)
$\delta\Delta_i\theta_l/\delta t_{diss}$	K h^{-1}	3.398	5.627 (3.571,13.27)
$\delta\mathrm{SHF}/\delta t_{diss}$	W m^{-2} h^{-1}	-26.35	-9.974 (-48.24,-5.562)
$\delta T_{sky}/\delta t_{diss}$	K h^{-1}	-8.556	-15.92 (-42.75,-9.781)
1D Trend	**Units**	**Cloud thickness variations ($h\|_{z_i}$)**	**Co-variability trends (95% CI)**
$\delta h/\delta t_{diss}$	m h^{-1}	78.74	319.6 (190.6,989.7)
2D Trend	**Units**	**Constant thickness variations ($z_i\|_h$)**	**Co-variability trends (95% CI)**
$\delta z_i/\delta t_{diss}$	m h^{-1}	320.9	171.1 (130.1,249.7)
$\delta q_t^{\mathrm{BL}}/\delta t_{diss}$	g kg^{-1} h^{-1}	-1.891	-21.11 (7.486,-4.380)

LIST OF FIGURES

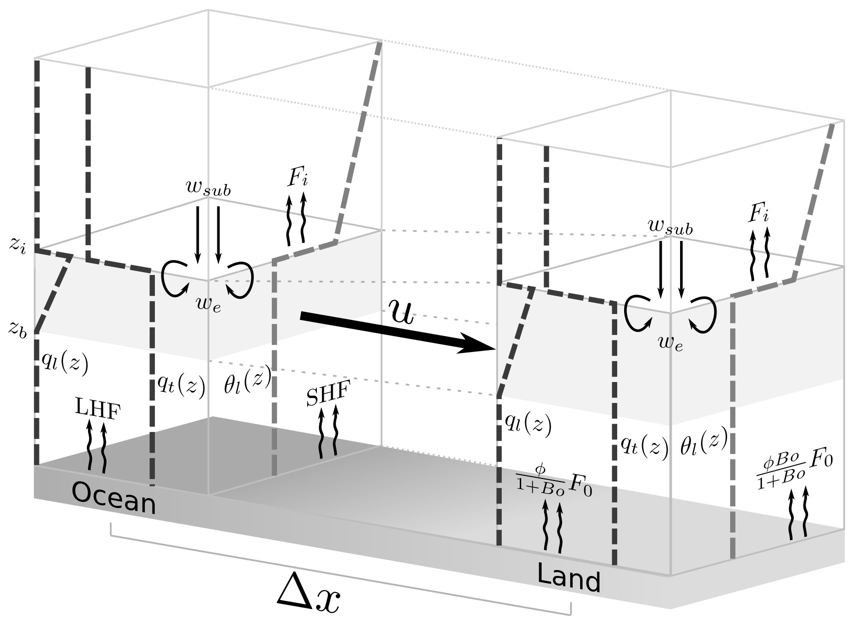

FIG. 1. Two columns are simulated to account for sea-breeze advection. Ocean and land column states are described by their height z_i, moisture $q_t(z)$, and temperature $\theta_l(z)$; from which the liquid water profile $q_l(z)$ and cloud-base height z_b can be derived. Ocean and land have different surface flux conditions, with the ocean having prescribed fluxes of LHF and SHF, while over land the net surface radiative flux F_0 is partitioned using a Bowen ratio Bo. At the cloud top, both columns are affected by the net radiative flux F_i and entrainment fluxes that depend on the inversion jumps. Entrainment mixes air into the columns at a rate w_e, while subsidence reduces column height at a rate w_{sub}. The properties of the ocean column are advected onto the land column with a wind speed u and considering a distance Δx (see Eq. B5).

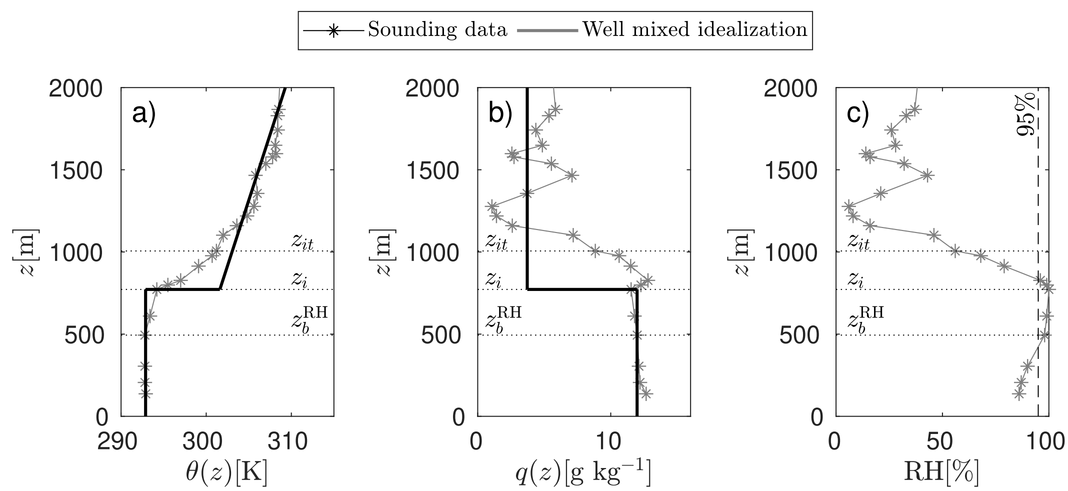

FIG. 2. Mixed-layer idealization for 21 July 2014. We detect the inversion region from radiosonde data (gray), and compute a well-mixed profile (black) by averaging properties in the ABL and tropospheric regions. The well-mixed profile is compatible with the MLM.

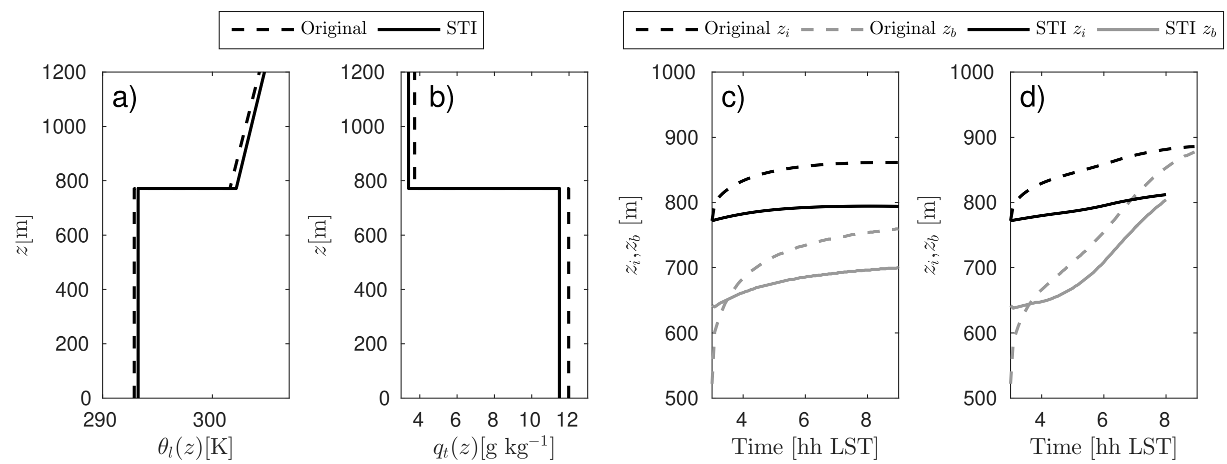

FIG. 3. Effect of the steady thickness initialization (STI) for 21 July 2014. The changes to the original sounding (dashed lines) for (a) $\theta_l(z)$ and (b) $q_t(z)$ are shown in solid lines. MLM simulated cloud boundaries z_i and z_b for the (c) ocean and (d) land column for the original properties and the modified STI.

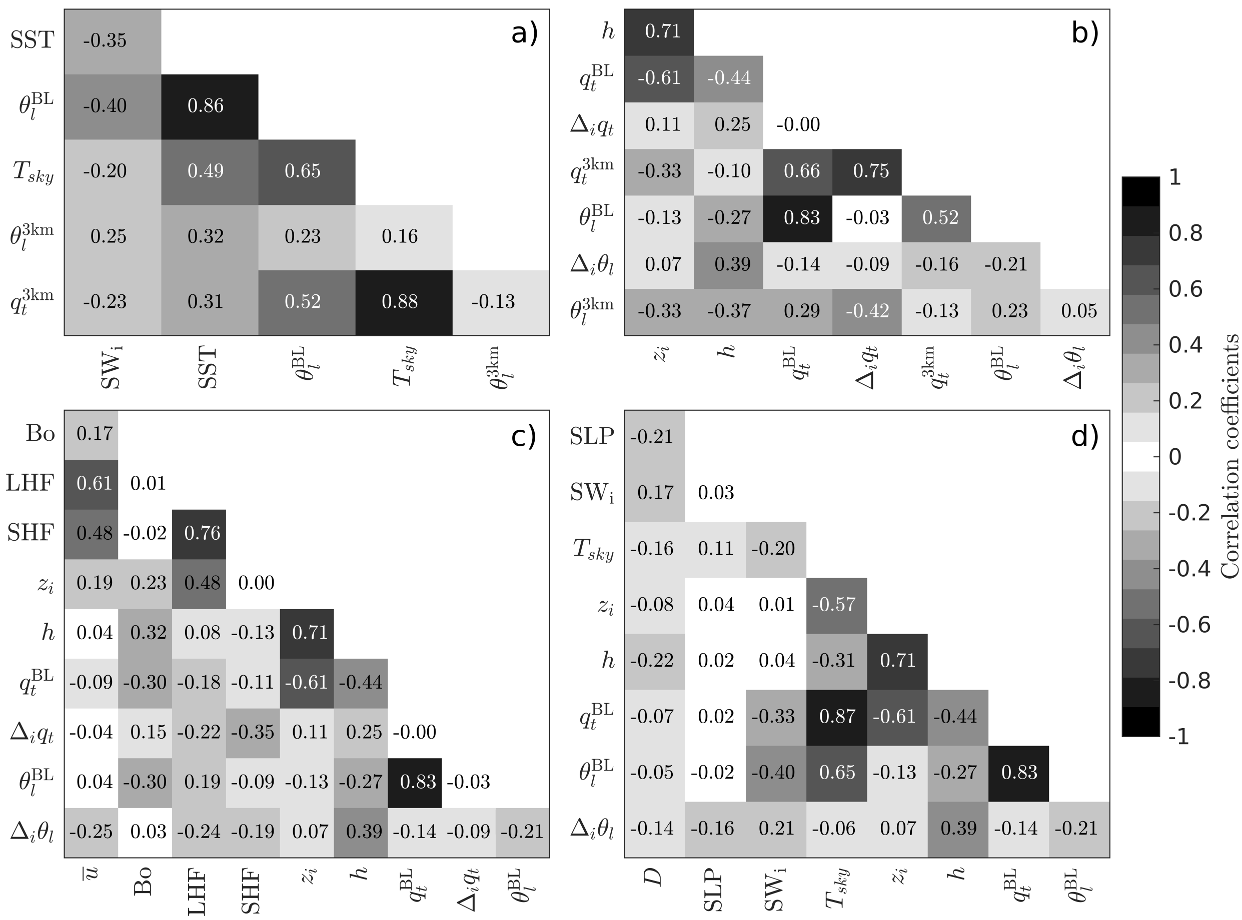

1103 FIG. 4. Correlation coefficient matrix for variables spanning the 195 selected days grouped by their relationship: (a) seasonal trends, (b) initial conditions, (c-d) boundary forcings divided into two figures for easier presentation: (c) wind and surface fluxes variables and (d) large scale and radiation parameters. The sign is representative of each correlation coefficient.

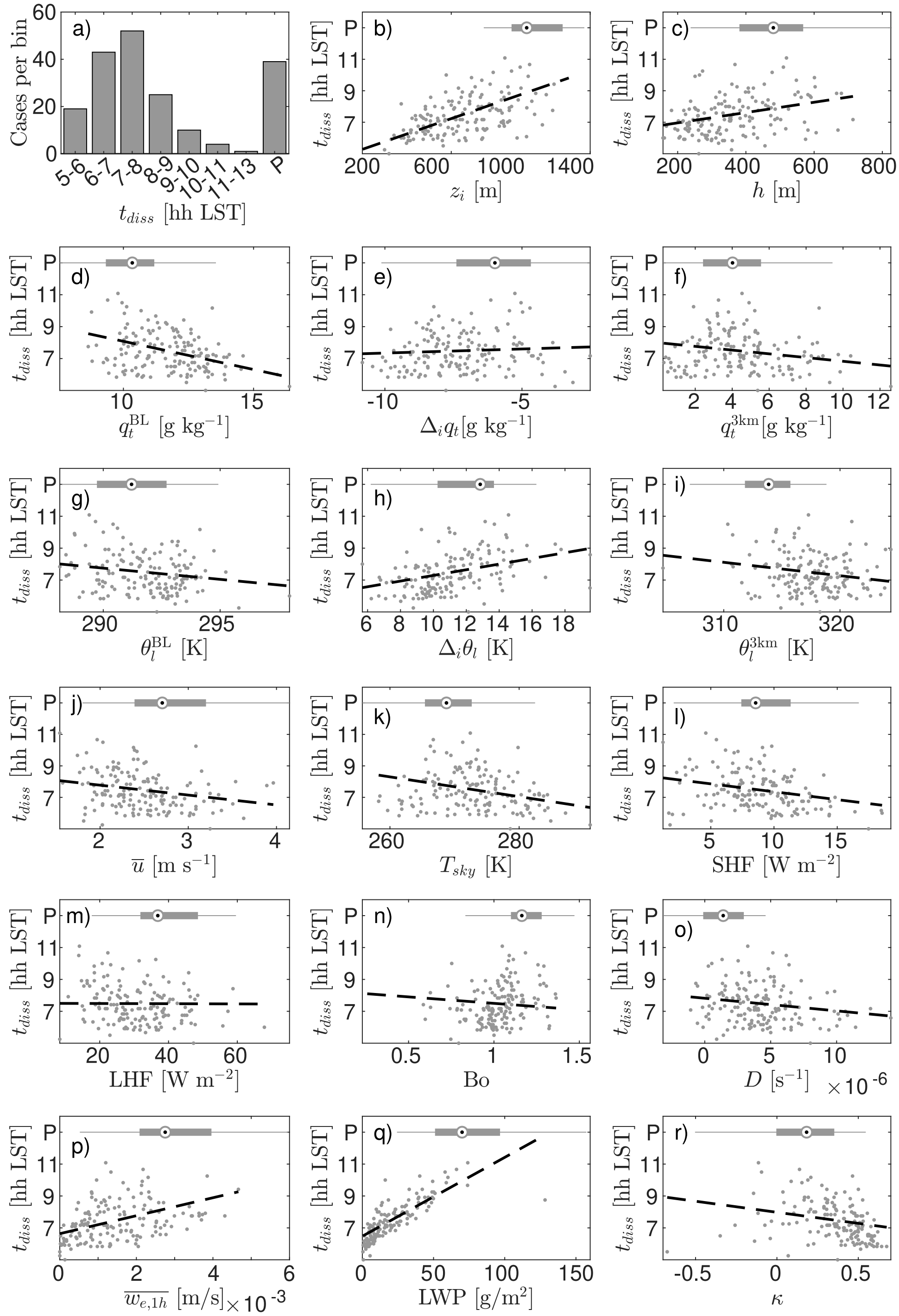

FIG. 5. (a) shows the distribution of dissipation time t_{diss} over coastal land. (b-r) show the effects of all variables on t_{diss} for all 195 days. Raw data (grey dots) and a linear fit (dashed black) are shown for the dissipating cases. Distributions (gray box plots) are shown for the persisting cases (marked as P in the t_{diss} axis), with boxes marking the 25 and 75 percentiles, circle marking the median, and lines extending between minimum and maximum (excluding outliers).

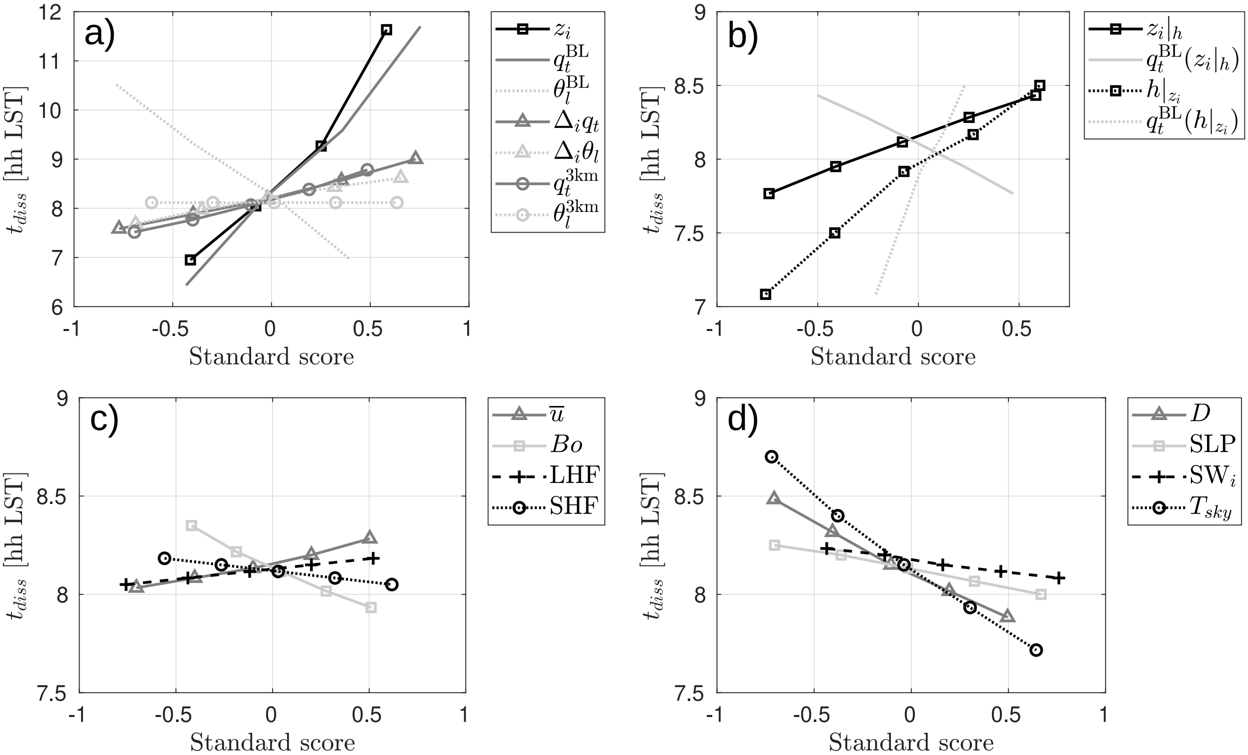

FIG. 6. Effect on dissipation time over land of the change of a single variable for the idealized reference case of observed medians. Variables are shown in terms of their Z-score, computed by subtracting the observed mean and dividing by the observed standard deviation. (a) Changes of initial condition variables one at a time, (b) changes of $z_i|_h$ to maintain constant cloud thickness and the corresponding values of $q_t^{\mathrm{BL}}(z_i|_h)$, and changes of $h|_{z_i}$ maintaining constant z_i and the corresponding changes of $q_t^{\mathrm{BL}}(h|_{z_i})$, (c) changes in advection and land surface forcing variables, (d) changes in radiative, subsidence and SLP variables. Some trends include less than five points as clouds were not present for some configurations.

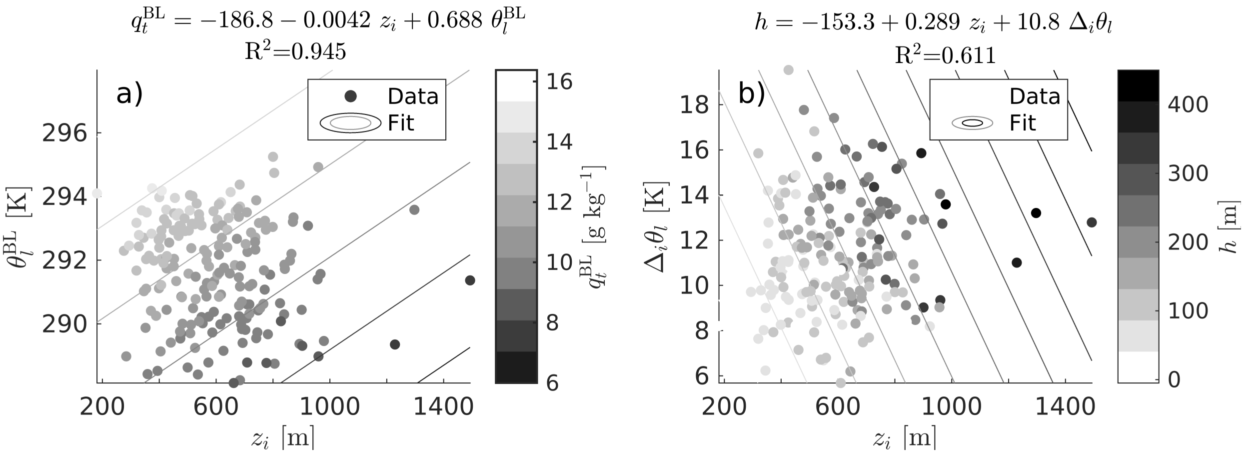

FIG. 7. Relationships between triads of variables: (a) q_t^{BL} in the plane described by z_i and θ_l^{BL}, and (b) h in the plane described by z_i and $\Delta_i\theta_l$. Gray dots are data points and contours are the best linear fit per the fit equation shown on top.

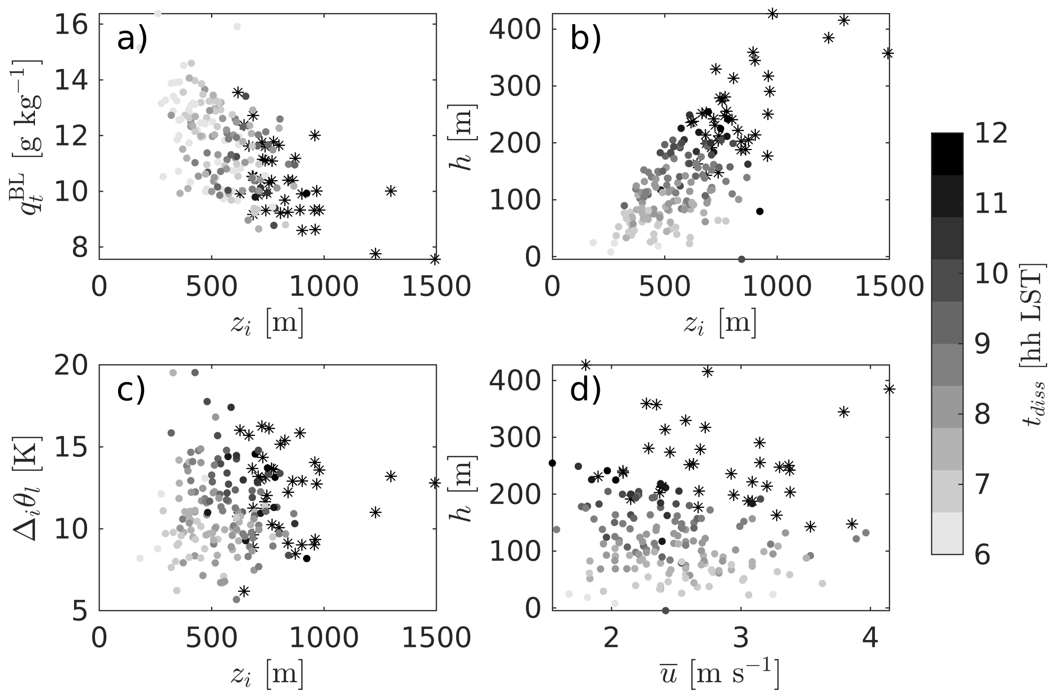

FIG. 8. Two-dimensional variable spaces for (a) z_i and q_t^{BL}, (b) z_i and h, (c) z_i and $\Delta_i\theta_l$, and (d) $\overline{u}$ and h. Data are classified by: cases that persist for the whole day (black asterisks, 38 cases), and cases that dissipate during the day (dots colored by dissipation time, 157 cases).

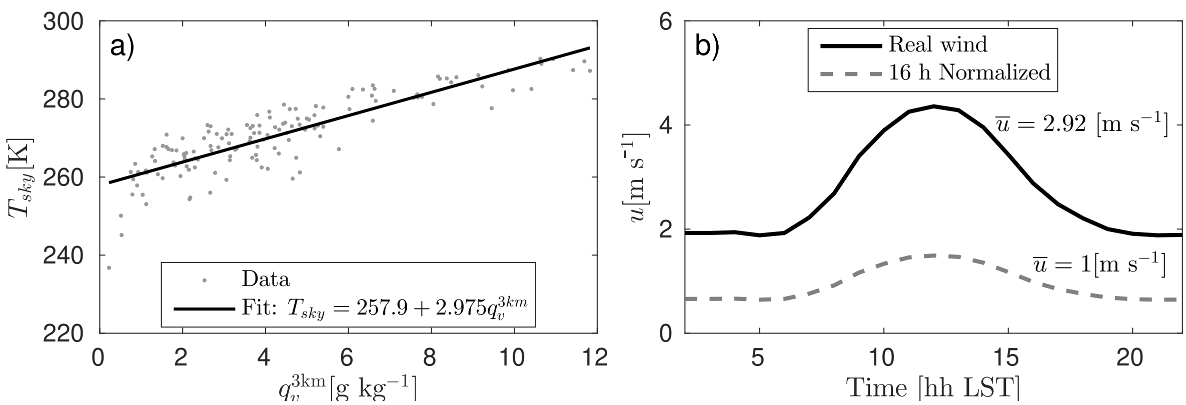

Fig. B1. (a) Sky effective radiative temperatures for the 209 cloudy days dataset as a function of water content above the cloud and below 3 km. The sky effective radiative temperatures were obtained with Streamer (Key and Schweiger 1998). (b) Climatological daily wind profile for the NKX station (10-year average), showing the original wind speed profile and the wind speed normalized by its 16 h average.

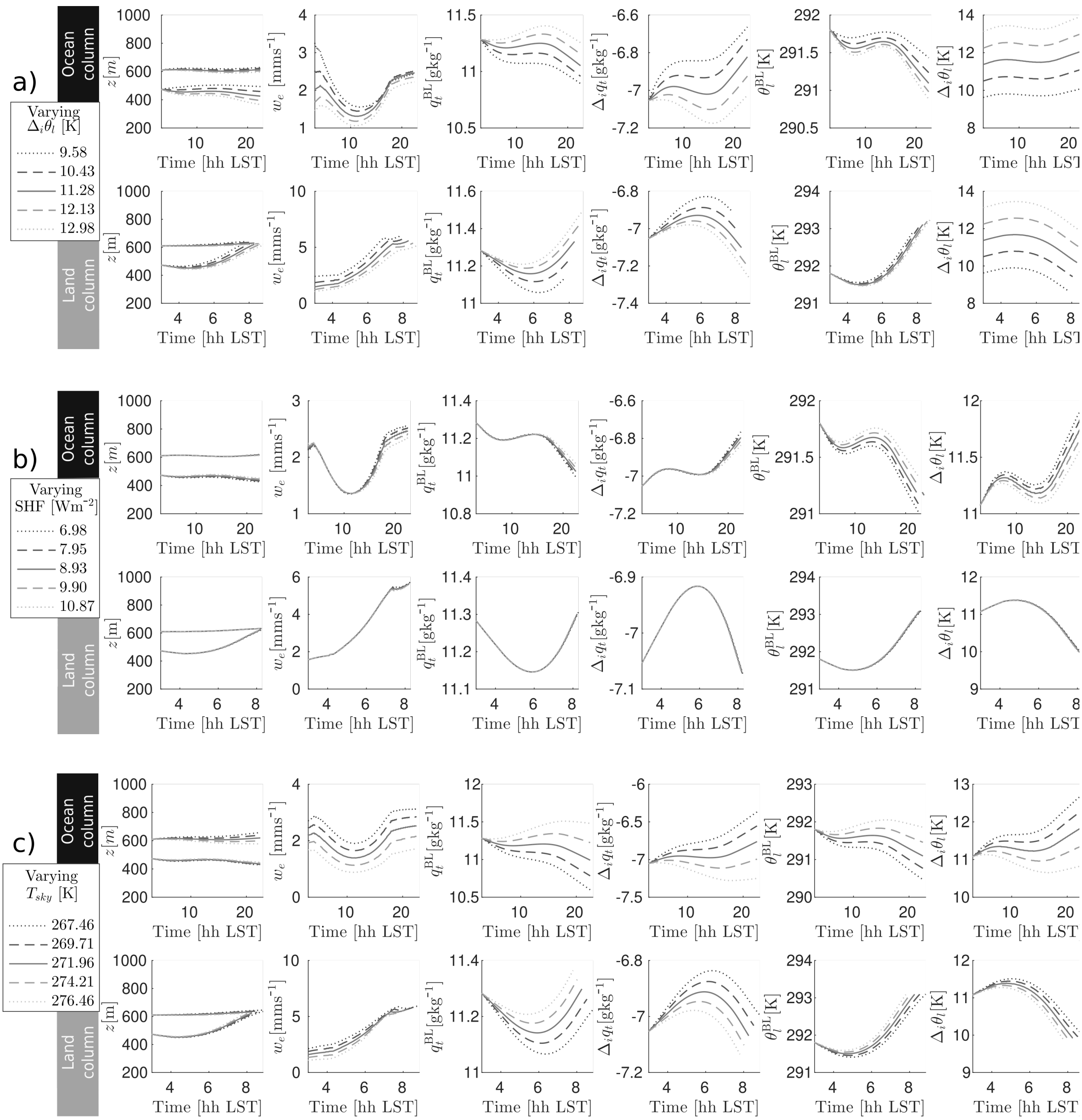

Fig. F1. Cloud evolution properties for the ocean (upper row) and land (lower row) columns, for single variable changes of (a) $\Delta_i\theta_l$, (b) SHF, and (c) T_{sky} over the idealized reference case. From left to right, they show: cloud boundaries, entrainment rate, q_t^{BL}, $\Delta_i q_t$, θ_l^{BL}, and $\Delta_i\theta_l$.